bioRxiv preprint doi: https://doi.org/10.1101/2020.05.11.089375; this version posted June 1, 2020. The copyright holder for this preprint (which was not certified by peer review) is the author/funder. All rights reserved. No reuse allowed without permission.

The SARS-CoV-2 conserved macrodomain is a highly efficient ADP-ribosylhydrolase

Yousef M.O. Alhammad[a], Maithri M. Kashipathy[b], Anuradha Roy[c], Jean-Philippe Gagné[d,e], Louis Nonfoux[d,e], Peter McDonald[c], Philip Gao[f], Kevin P. Battaile[g], David K. Johnson[h], Guy G. Poirier[d,e], Scott Lovell[b] and Anthony R. Fehr[a,#]

[a]Department of Molecular Biosciences, University of Kansas, Lawrence, Kansas 66045, USA
[b]Protein Structure Laboratory, University of Kansas, Lawrence, Kansas 66047, USA
[c]High Throughput Screening Laboratory, University of Kansas, Lawrence, Kansas 66047, USA
[d]Department of Molecular Biology, Medical Biochemistry and Pathology, Laval University Cancer Research Center, Québec City, QC, G1V 0A6, Canada
[e]CHU de Québec Research Center, CHUL Pavilion, Oncology Division, Québec City, QC, G1V 4G2, Canada
[f]Protein Production Group, University of Kansas, Lawrence, Kansas 66047, USA
[g]NYX, New York Structural Biology Center, Upton, NY 11973, USA
[h]Molecular Graphics and Modeling Laboratory and the Computational Chemical Biology Core, University of Kansas, Lawrence, Kansas 66047, USA

[#]Correspondence: arfehr@ku.edu; Tel.: +1- (785) 864-6626 (K.S.)

Running title: SARS-CoV-2 Mac1 removes ADP-ribose from protein

Keywords: Coronavirus, SARS-CoV-2, macrodomain, ADP-ribose, poly-ADP-ribose,

bioRxiv preprint doi: https://doi.org/10.1101/2020.05.11.089375; this version posted June 1, 2020. The copyright holder for this preprint (which was not certified by peer review) is the author/funder. All rights reserved. No reuse allowed without permission.

ABSTRACT

Severe acute respiratory syndrome coronavirus 2 (SARS-CoV-2) and other SARS-like-CoVs encode 3 tandem macrodomains within non-structural protein 3 (nsp3). The first macrodomain, Mac1, is conserved throughout CoVs, binds to and hydrolyzes mono-ADP-ribose (MAR) from target proteins. Mac1 likely counters host-mediated anti-viral ADP-ribosylation, a posttranslational modification that is part of the host response to viral infections. Mac1 is essential for pathogenesis in multiple animal models of CoV infection, implicating it as a virulence factor and potential therapeutic target. Here we report the crystal structure of SARS-CoV-2 Mac1 in complex with ADP-ribose. SARS-CoV-2, SARS-CoV and MERS-CoV Mac1 exhibit similar structural folds and all 3 proteins bound to ADP-ribose with low μM affinities. In contrast, we found that only the MERS-CoV Mac1 protein bound to poly-ADP-ribose (PAR), and none of these enzymes could hydrolyze PAR. Importantly, using ADP-ribose detecting antibodies and both gel-based assay and novel ELISA assays, we demonstrated highly efficient de-MARylating activity for all 3 CoV Mac1 proteins. We conclude that the SARS-CoV-2 and other CoV Mac1 proteins are highly efficient MAR-hydrolases with strikingly similar activity, indicating that compounds targeting CoV Mac1 proteins may have broad anti-CoV activity.

bioRxiv preprint doi: https://doi.org/10.1101/2020.05.11.089375; this version posted June 1, 2020. The copyright holder for this preprint (which was not certified by peer review) is the author/funder. All rights reserved. No reuse allowed without permission.

IMPORTANCE

SARS-CoV-2 has recently emerged into the human population and has led to a worldwide pandemic of COVID-19 that has caused nearly 350 thousand deaths worldwide. With, no currently approved treatments, novel therapeutic strategies are desperately needed. All coronaviruses encode for a highly conserved macrodomain (Mac1) that binds to and removes ADP-ribose adducts from proteins in a dynamic post-translational process increasingly recognized as an important factor that regulates viral infection. The macrodomain is essential for CoV pathogenesis and may be a novel therapeutic target. Thus, understanding its biochemistry and enzyme activity are critical first steps for these efforts. Here we report the crystal structure of SARS-CoV-2 Mac1 in complex with ADP-ribose, and describe its ADP-ribose binding and hydrolysis activities in direct comparison to SARS-CoV and MERS-CoV Mac1 proteins. These results are an important first step for the design and testing of potential therapies targeting this unique protein domain.

bioRxiv preprint doi: https://doi.org/10.1101/2020.05.11.089375; this version posted June 1, 2020. The copyright holder for this preprint (which was not certified by peer review) is the author/funder. All rights reserved. No reuse allowed without permission.

INTRODUCTION

The recently emerged pandemic outbreak of COVID-19 is caused by a novel coronavirus named severe acute respiratory syndrome coronavirus 2 (SARS-CoV-2) (1, 2). As of May 28, 2020, this virus has been responsible for ~ 5.7 million cases of COVID-19 and >350,000 deaths worldwide. SARS-CoV-2 is a member of the lineage B β-CoVs with overall high sequence similarity with other SARS-like CoVs, including SARS-CoV. While most of the genome is >80% similar with SARS-CoV, there are regions where amino acid conservation is significantly lower. As expected, the most divergent proteins in the SARS-CoV-2 genome from SARS-CoV include the Spike glycoprotein and several accessory proteins including 8a (absent), 8b (extended), and 3b (truncated). However, somewhat unexpectedly, several non-structural proteins also show significant divergence from SARS-CoV, including non-structural proteins 3, 4, and 7, which could affect the biology of SARS-CoV-2 (3, 4).

Coronaviruses encode 16 non-structural proteins that are translated from two open reading frames (ORFs), replicase 1a and 1ab (rep1a and rep1ab) (5). The largest non-structural protein is the non-structural protein 3 (nsp3) that encodes for multiple modular protein domains. These domains in SARS-CoV-2 diverge in amino acid sequence from SARS-CoV as much as 30%, and SARS-CoV-2 nsp3 includes a large insertion of 25-41 residues just upstream of the first of three tandem macrodomains (Mac1, Mac2, and Mac3) (Fig. 1A) (3). In addition to this insertion, the individual macrodomains show large amounts of amino acid divergence. Mac1 diverges 28% from SARS-CoV and 59% from MERS-CoV, while Mac2 and Mac3 diverge 24% from SARS-CoV. It is feasible that these significant sequence differences could impact the unique biology of SARS-CoV-2. However, macrodomains have a highly conserved structure, and thus sequence divergence may have little impact on their overall function. Mac1 is present in

bioRxiv preprint doi: https://doi.org/10.1101/2020.05.11.089375; this version posted June 1, 2020. The copyright holder for this preprint (which was not certified by peer review) is the author/funder. All rights reserved. No reuse allowed without permission.

all CoVs, unlike Mac2 and Mac3, and early structural and biochemical data demonstrated that it contains a conserved three-layered α/β/α fold and binds to mono-ADP-ribose (MAR), poly-ADP-ribose (PAR), and other related molecules (6-10). ADP-ribose is buried in a hydrophobic cleft where the ADP-ribose binds to several highly-conserved residues such as aspartic acid at position 23 (D23) and asparagine at position 41 (N41) of SARS-CoV (6). Mac1 homologs are also found in alphaviruses, Hepatitis E virus, and Rubella virus, and structural analysis of these macrodomains have demonstrated that they are very similar to CoV Mac1 (11, 12). All are members of the larger MacroD-type macrodomain family, which includes human macrodomains Mdo1 and Mdo2 (13).

The CoV Mac1 was originally named ADP-ribose-1”-phosphatase (ADRP) based on data demonstrating that it could remove the phosphate group from ADP-ribose-1”-phosphate (6-8). However, the activity was rather modest, and it was unclear why this would impact a virus infection. More recently it has been demonstrated that CoV Mac1 can hydrolyze the bond between amino acid chains and ADP-ribose molecules (14-16), indicating that it can reverse protein ADP-ribosylation (6, 8). ADP-ribosylation is a post-translational modification catalyzed by ADP-ribosyltransferases (ARTs, also known as PARPs) through transferring an ADP-ribose moiety from NAD^+ onto target proteins (17). The ADP-ribose is transferred as a single units of MAR, or single units of MAR are transferred consecutively to form a PAR chain. CoV Mac1 proteins hydrolyze MAR, but have minimal activity against PAR (14, 15). Several MARylating PARPs are induced by interferon (IFN) and are known to inhibit virus replication, implicating MARylation in the host-response to infection (18).

Several reports have addressed the role of Mac1 on the replication and pathogenesis of CoVs, mostly using the mutation of a highly conserved asparagine to alanine. This mutation

bioRxiv preprint doi: https://doi.org/10.1101/2020.05.11.089375; this version posted June 1, 2020. The copyright holder for this preprint (which was not certified by peer review) is the author/funder. All rights reserved. No reuse allowed without permission.

abolished the MAR-hydrolase activity of SARS-CoV Mac1 (16). This mutation has minimal effects on CoV replication in transformed cells, but reduces viral load, leads to enhanced IFN production, and strongly attenuates both Murine Hepatitis Virus (MHV) and SARS-CoV in mouse models of infection (7, 16, 19, 20). MHV Mac1 was also required for efficient replication in primary macrophages, which could be partially rescued by the PARP inhibitors XAV-939 and 3-AB or siRNA knockdown of PARP12 or PARP14 (21). These data suggest that Mac1's likely function is to counter PARP-mediated anti-viral ADP-ribosylation (22). Mutations in the alphavirus and HEV macrodomain also have substantial phenotypic effects on virus replication and pathogenesis (14, 23-26). As viral macrodomains are clearly important virulence factors, they are considered to be potential targets for anti-viral therapeutics (22).

Based on the close structural similarities between viral macrodomains, we hypothesized that SARS-CoV-2 Mac1 has similar binding and hydrolysis activity as other CoV Mac1 enzymes. In this study, we determined the crystal structure of the SARS-CoV-2 Mac1 protein bound to ADP-ribose. Binding to MAR and PAR was tested and directly compared to a human macrodomain (Mdo2) and the SARS-CoV and MERS-CoV Mac1 proteins by several *in vitro* assays. All CoV Mac1 proteins bound to MAR with similar affinity, but only the MERS-CoV Mac1 could bind to PAR. Finally, we demonstrated that SARS-CoV-2, SARS-CoV, and MERS-CoV Mac1 proteins could efficiently remove MAR from a protein substrate, but did not remove PAR. These results indicate very similar function for CoV Mac1 proteins, and will be instrumental in the design and testing of novel therapeutic agents targeting the CoV Mac1 protein domain.

bioRxiv preprint doi: https://doi.org/10.1101/2020.05.11.089375; this version posted June 1, 2020. The copyright holder for this preprint (which was not certified by peer review) is the author/funder. All rights reserved. No reuse allowed without permission.

RESULTS

Structure of the SARS-CoV-2 Mac1 complexed with ADP-ribose. To create recombinant SARS-CoV-2 Mac1 for structure determination and enzyme assays, nucleotides 3348-3872 of SARS-CoV-2 isolate Wuhan-hu-1 (accession number NC_045512), representing amino acids I1023-K1197 of rep1a, were cloned into a bacterial expression vector containing an N-terminal 6X-His tag and TEV cleavage site. We obtained large amounts (>100 mg) of purified recombinant protein (Fig. S1A). A small amount of this protein was digested by the TEV protease to obtain protein devoid of any extra tags for crystallization and used to obtain crystals from which the structure was determined (Fig. S1B). Our crystallization experiments resulted in the same crystal form (needle clusters) from several conditions, but only when ADP-ribose was added to the protein. This represents an additional crystal form ($P2_1$) amongst the recently determined SARS-CoV-2 macrodomain structures (27-29).

The structure of SARS-CoV-2 Mac1 complexed with ADP-ribose was obtained using X-ray diffraction data to 2.2 Å resolution and contained four molecules in the asymmetric unit that were nearly identical. The polypeptide chains could be traced from V3-M171 for subunits A/C and V3-K172 for subunits B/D. Superposition of subunits B-D onto subunit A (169 residues aligned) yielded RMSD deviations of 0.17 Å, 0.17 Å and 0.18 Å respectively between Cα atoms. As such, subunit A was used for the majority of the structure analysis described herein. The SARS-CoV-2 Mac1 protein adopted a fold consistent with the MacroD subfamily of macrodomains that contains a core composed of a mixed arrangement of 7 β-sheets (parallel and antiparallel) that are flanked by 6 α-helices (Fig. 2A-B).

As mentioned above, apo crystals were never observed for our construct, though the apo structure has been solved by researchers at The Center for Structural Genomics of Infectious

bioRxiv preprint doi: https://doi.org/10.1101/2020.05.11.089375; this version posted June 1, 2020. The copyright holder for this preprint (which was not certified by peer review) is the author/funder. All rights reserved. No reuse allowed without permission.

Diseases (PDB 6WEN) (28) and the University of Wisconsin-Milwaukee (PDB 6WEY) (27). Further analysis of the amino acid sequences used for expression and purification revealed that our construct had 5 additional residues at the C-terminus (MKSEK) and differs slightly at the N-terminus as well (GIE vs GE) relative to 6WEN. In addition, the sequence used to obtain the structure of 6WEY is slightly shorter than SARS-CoV-2 Mac1 at both the N and C-terminal regions (Fig. S2A). To assess the effect of these additional residues on crystallization, chain B of the SARS-CoV-2 Mac1, which was traced to residue K172, was superimposed onto subunit A of PDB 6W02 (29), a previously determined structure of ADP-ribose bound SARS-CoV-2 Mac1. Analysis of the crystal packing of 6W02 indicates that the additional residues at the C-terminus would clash with symmetry related molecules (Fig. S2B). This suggests that the presence of these extra residues at the C-terminus likely prevented the generation of the more tightly packed crystal forms obtained for 6W02 and 6WEY, which diffracted to high resolution.

The ADP-ribose binding pocket contained large regions of positive electron density consistent with ADP-ribose molecules (Fig. 3A). The adenine forms two hydrogen bonds with D22-I23, which makes up a small loop between β2 and the N-terminal half of α1. The side chain of D22 interacts with N6, while the backbone nitrogen atom of I23 interacts with N1, in a very similar fashion to the SARS-CoV macrodomain (6). A large number of contacts are made in the loop between β3 and α2 which includes many highly-conserved residues, including a GGG (motif) and N40, which is completely conserved in all enzymatically active macrodomains (30). N40 is positioned to make hydrogen bonds with the 3' OH groups of the distal ribose, as well as a conserved water molecule. K44 and G46 also make hydrogen bonds with the 2' OH of the distal ribose, G48 makes contact with the 1' OH and a water that resides near the catalytic site, while the backbone nitrogen atom of V49 hydrogen bonds with the α-phosphate. The other major

bioRxiv preprint doi: https://doi.org/10.1101/2020.05.11.089375; this version posted June 1, 2020. The copyright holder for this preprint (which was not certified by peer review) is the author/funder. All rights reserved. No reuse allowed without permission.

interactions with ADP-ribose occur in residues G130, I131, and F132 that are in the loop between β6 and α5 (Fig. 3B). The α-phosphate accepts a hydrogen bond from the nitrogen atom of I131, while the β-phosphate accepts hydrogen bonds from the backbone nitrogen atom of G130 and F132. Loops β3-α2 and β6-α5 are connected by an isoleucine bridge that forms a narrow channel around the diphosphate which helps position the terminal ribose for water-mediated catalysis (6). Additionally, a network of direct contacts of ADP-ribose to solvent along with water mediated contacts to the protein are shown (Fig. 3C).

Comparison of SARS-CoV-2 Mac1 with other CoV macrodomain structures. We next sought to compare the SARS-CoV-2 Mac1 to other deposited structures of this protein. Superposition with Apo (6WEN) and ADP-ribose complexed protein (6W02) yielded RMSD of 0.48 Å (168 residues) and 0.37 Å (165 residues), respectively, indicating a high degree of similarity (Fig. S3A-B). Comparison of the ADP-ribose binding site of SARS-CoV-2 Mac1 with that of the apo structure (6WEN) revealed minor conformational differences in order to accommodate ADP-ribose binding. The loop between β3 and α2 (H45-V49) undergoes a change in conformation and the sidechain of F132 is moved out of the ADP-ribose binding site (Fig. S3C). Our ADP-ribose bound structure is nearly identical to 6W02, except for slight deviations in the β3-α2 loop and an altered conformation of F156, where the aryl ring of F156 is moved closer to the adenine ring (Fig. S3 C-D). However, this is likely a result of crystal packing as F156 adopts this conformation in each subunit and would likely clash with subunit residues related by either crystallographic or non-crystallographic symmetry.

We next compared the ADP-ribose bound SARS-CoV-2 Mac1 structure with that of SARS-CoV (PDB 2FAV) (6) and MERS-CoV (PDB 5HOL) (31) Mac1 proteins. Superposition yielded RMSD deviations of 0.71 Å (166 residues) and 1.06 Å (161 residues) for 2FAV and

bioRxiv preprint doi: https://doi.org/10.1101/2020.05.11.089375; this version posted June 1, 2020. The copyright holder for this preprint (which was not certified by peer review) is the author/funder. All rights reserved. No reuse allowed without permission.

191 5HOL, respectively. Additionally, the ADP-ribose binding mode in the SARS-CoV and SARS-
192 CoV-2 structures almost perfectly superimposed (Fig. 4A-D). The conserved aspartic acid
193 residue (D22, SARS-CoV-2) that binds to adenine, are localized in a similar region although
194 there are slight differences in the rotamers about the Cβ-Cγ bond. The angles between the mean
195 planes defined by the OD1, CG and OD2 atoms relative to SARS-CoV-2 Mac1 is 23.1° and
196 46.5° for the SARS-CoV and MERS-CoV Mac1 structures, respectively. Another notable
197 difference is that SARS-CoV and SARS-CoV-2 macrodomains have an isoleucine (I23)
198 following this aspartic acid while MERS-CoV has an alanine (A22). Conversely, SARS-CoV-2
199 and SARS-CoV Mac1 have a valine instead of an isoleucine immediately following the GGG
200 motif (V49/I48). From these structures it appears that having two isoleucines in this location
201 would clash, and that lineage B and lineage C β-CoVs has evolved in unique ways to create
202 space in this pocket (Fig. 4D and data not shown). Despite these small differences in local
203 structure, the overall structure of CoV Mac1 domains remain remarkably conserved, and
204 indicates they likely have similar biochemical activities and biological functions.

205 **SARS-CoV, SARS-CoV-2, and MERS-CoV bind to ADP-ribose with similar**
206 **affinities.** To determine if the CoV macrodomains had any noticeable differences in their ability
207 to bind ADP-ribose, we performed isothermal titration calorimetry (ITC), which measures the
208 energy released or absorbed during a binding reaction. Macrodomain proteins from human
209 (Mdo2), SARS-CoV, MERS-CoV, and SARS-CoV-2 were purified (Fig. S1A) and tested for
210 their affinity to ADP-ribose. All CoV Mac1 proteins bound to ADP-ribose with low micromolar
211 affinity (7-16 μM), while human Mdo2 bound with an affinity about 10-times stronger (~220
212 nM) (Fig. 5A-B). As a control we tested the ability of the MERS-CoV macrodomain to bind to
213 ATP, and only observed minimal binding with mM affinity (data not shown). At higher

bioRxiv preprint doi: https://doi.org/10.1101/2020.05.11.089375; this version posted June 1, 2020. The copyright holder for this preprint (which was not certified by peer review) is the author/funder. All rights reserved. No reuse allowed without permission.

concentrations, the SARS-CoV-2 macrodomain caused a slightly endothermic reaction, potentially the result of protein aggregation or a change in conformation (Fig. 5A). The MERS-CoV Mac1 had a greater affinity for ADP-ribose than SARS-CoV or SARS-CoV-2 Mac1 in the ITC assay (Fig. 5A-B), however, our results found the differences between these macrodomain proteins to be much closer than previously reported (9). As an alternate method to confirm ADP-ribose binding, we conducted a thermal shift assay. All 4 macrodomains tested denatured at higher temperatures with the addition of ADP-ribose (Fig. S4). We then tested the ability of the CoV Mac1 proteins to bind to PAR using a PAR overlay assay. Macrodomain proteins were slot-blotted onto a nitrocellulose membrane and were then incubated with purified PAR. PAR binding was then detected with 2 distinct anti-PAR antibodies (Fig. 5C). Histone H1, which binds very efficiently to PAR, and DNaseI were used as positive and negative controls, respectively, as described previously (32). This assay showed that Mdo2 and MERS-CoV Mac1 could bind to PAR, in contrast to SARS-CoV or SARS-CoV-2 Mac1, which were unable to bind PAR. Importantly, only 1 pmol of Histone H1 was needed to bind to PAR, while 60 pmol of the macrodomain proteins were used to detect PAR binding. We conclude that lineage B and lineage C β-CoV Mac1 proteins bind to ADP-ribose with similar affinities, but demonstrate unique differences in their ability to bind PAR.

CoV macrodomains are highly efficient MAR-hydrolases. To examine the MAR-hydrolase activity of CoV Mac1, we first tested the viability of using antibodies to detect MARylated protein. Previously, radiolabeled NAD^+ has been the primary method used to label MARylated protein (14, 15). To create a MARylated substrate, the catalytic domain of the PARP10 (GST-PARP10 CD) protein was incubated with NAD^+, leading to its automodification. We then tested a panel of monoclonal antibodies that detect MAR, PAR, or both MAR and PAR

bioRxiv preprint doi: https://doi.org/10.1101/2020.05.11.089375; this version posted June 1, 2020. The copyright holder for this preprint (which was not certified by peer review) is the author/funder. All rights reserved. No reuse allowed without permission.

for the ability to detect MARylated PARP10. The anti-MAR and anti-MAR/PAR antibodies, but not anti-PAR antibody, bound to MARylated PARP10 (Fig. S5). From herein we utilized the anti-MAR antibody to detect MARylated PARP10.

We next tested the ability of SARS-CoV-2 Mac1 to remove ADP-ribose from MARylated PARP10. SARS-CoV-2 Mac1 and MARylated PARP10 were incubated at equimolar amounts of protein at 37°C and the reaction was stopped at 5, 10, 20, 30, 45 or 60 minutes (Fig. 6A). As a control, MARylated PARP10 was incubated alone for 60 minutes at 37°C. Each reaction had equivalent amounts of MARylated PARP10 and Mac1 which was confirmed by Coomassie Blue staining (Fig. 6A). An immediate reduction of more than 50% band intensity was observed within five minutes, and the ADP-ribose modification was nearly completely removed by SARS-CoV-2 Mac1 within 30 minutes (Fig. 6A). The MARylated PAPR10 bands intensities were calculated, plotted, and fit to a non-linear regression curve (Fig. 6B). This result indicates that the SARS-CoV-2 Mac1 protein is a highly efficient MAR-hydrolase.

Next, we compared MAR-hydrolase activity of Mac1 from SARS-CoV-2, SARS-CoV, and MERS-CoV and human Mdo2. These proteins were incubated with MARylated PARP10 as described above and the removal of MAR was analyzed at 5, 15 and 30 minutes (Fig. 6C). MAR was rapidly removed from MARylated PARP10 with the CoV Mac1 proteins (Fig. 6D). Approximately 95% of MAR was removed by SARS-CoV and SARS-CoV-2 Mac1 within 15 minutes, while at the same timepoint MERS-CoV Mac1 removed about 85% of MAR (Fig. 6D). A more gradual decrease of MARylated PAPR10 band intensity was observed with Mdo2. It removed approximately 70% of MAR in 30 minutes, which was significantly different from both SARS-CoV and SARS-CoV-2 Mac1. These data showed that CoV Mac1 proteins have similar

bioRxiv preprint doi: https://doi.org/10.1101/2020.05.11.089375; this version posted June 1, 2020. The copyright holder for this preprint (which was not certified by peer review) is the author/funder. All rights reserved. No reuse allowed without permission.

MAR-hydrolase activity against an auto-modified PARP10 protein, and they have increased activity when compared to the human Mdo2 protein under these conditions. However, further enzymatic analyses of these proteins are warranted to more thoroughly understand their kinetics and affinities for various MARylated substrates.

CoV Mac1 proteins do not hydrolyze PAR. To determine if the CoV Mac1 proteins could remove PAR from proteins, we incubated these proteins with an auto-PARylated PARP1 protein. PARP1 was incubated with increasing concentrations of NAD^+ to create a range of modification levels (Fig. S6). We incubated both partially and heavily modified PARP1 with all four macrodomains and PARG as a positive control for 1 hour. While PARG completely removed PAR, none of the macrodomain proteins removed PAR chains from PARP1 (Fig. 6E). We conclude that macrodomain proteins are unable to remove PAR from an automodified PARP1 protein under these conditions.

ELISA assays can be used to measure ADP-ribosylhydrolase activity of macrodomains. Gel based assays as described above suffer from significant limitations in the number of samples that can be done at once. A higher throughput assay will be needed to more thoroughly investigate the activity of these enzymes and to screen for inhibitor compounds. Based on the success of our antibody-based detection of MAR, we developed an ELISA assay that has a similar ability to detect de-MARylation as our gel-based assay, but with the ability to do so in a higher throughput manner (Fig. 7A). First, MARylated PARP10 was added to ELISA plates. Next, the wells were washed and then incubated with different concentrations of the SARS-CoV-2 Mac1 protein for 30 min. After incubation, the wells were washed and treated with anti-MAR antibody, followed by HRP-conjugated secondary antibody and the detection reagent. As controls, we detected MARylated and non-MARylated PARP10 proteins bound to

bioRxiv preprint doi: https://doi.org/10.1101/2020.05.11.089375; this version posted June 1, 2020. The copyright holder for this preprint (which was not certified by peer review) is the author/funder. All rights reserved. No reuse allowed without permission.

283 glutathione plates with anti-GST and anti-MAR antibodies as primary and their corresponding
284 secondary antibodies (Fig. 7B). SARS-CoV-2 Mac1 was able to remove MAR signal in a dose-
285 dependent manner and fit to a non-linear regression curve (Fig. 7C). Based on these results, we
286 conclude that this ELISA assay will be a useful tool for screening potential inhibitors or defining
287 enzyme kinetics of macrodomain proteins.

bioRxiv preprint doi: https://doi.org/10.1101/2020.05.11.089375; this version posted June 1, 2020. The copyright holder for this preprint (which was not certified by peer review) is the author/funder. All rights reserved. No reuse allowed without permission.

DISCUSSION

Here we report the crystal structure of SARS-CoV-2 Mac1 and its enzyme activity *in vitro*. Structurally, it has a conserved three-layered α/β/α fold typical of the MacroD family of macrodomains, and is extremely similar to other CoV Mac1 proteins (Fig. 2-4). The conserved CoV macrodomain (Mac1) was initially described as an ADP-ribose-1”-phosphatase (ADRP), as it was shown to be structurally similar to yeast enzymes that have this enzymatic activity (33). Early biochemical studies confirmed this activity for CoV Mac1, though its phosphatase activity for ADP-ribose-1”-phosphate was rather modest (6-8). Later, it was shown that mammalian macrodomain proteins could remove ADP-ribose from protein substrates, indicating protein de-ADP-ribosylation as a more likely function for the viral macrodomains (30, 34, 35). Shortly thereafter, the SARS-CoV, hCoV-229E, FIPV, several alphavirus, and the hepatitis E virus macrodomains were demonstrated to have de-ADP-ribosylating activity (14-16). However, this activity has not yet been reported for the MERS-CoV or SARS-CoV-2 Mac1 protein.

In this study, we show that the Mac1 proteins from SARS-CoV, MERS-CoV and SARS-CoV-2 hydrolyze MAR from a protein substrate (Fig. 6). Their activities were similar despite sequence divergence of almost 60% between SARS-CoV-2 and MERS-CoV. We then compared these activities to the human Mdo2 macrodomain. Mdo2 had a greater affinity for ADP-ribose than the viral enzymes, but had significantly reduced enzyme activity in our experiments. However, it’s possible that the Mdo2 and potentially the MERS-CoV Mac1 proteins were partially inhibited by the released MAR in these assays due to their tighter binding to ADP-ribose. Regardless, these results suggest that the human and viral enzymes likely have structural differences that result in alterations in their biochemical activities *in vitro*.

bioRxiv preprint doi: https://doi.org/10.1101/2020.05.11.089375; this version posted June 1, 2020. The copyright holder for this preprint (which was not certified by peer review) is the author/funder. All rights reserved. No reuse allowed without permission.

We also compared the ability of these macrodomain proteins to bind and hydrolyze PAR. None of the macrodomains were able to hydrolyze either partially or heavily modified PARP1, further demonstrating that the primary enzyme activity of these proteins is to hydrolyze MAR (Fig. 6E). Intriguingly, the Mdo2 and MERS-CoV macrodomain proteins bound to poly-ADP-ribose, while the SARS-CoV-2 and SARS-CoV proteins did not (Fig. 5C). It is unclear if this binding is relevant during infection, as these proteins do not bind to PAR nearly as well as prominent PAR binding proteins, such as Histone H1, APFL, CHFR, DNA ligase 3, and XRCC1 (Fig. 5C) (36). From a structural standpoint it is unclear why MERS-CoV would bind PAR while the other CoV Mac1 proteins do not. Further investigation is needed to understand the PAR binding ability of these macrodomains, such as determining the length of PAR chains they bind to, and if it is relevant for their true biological functions.

While all previous studies of macrodomain de-ADP-ribosylation have primarily used radiolabeled substrate, we obtained highly repeatable and robust data utilizing antibodies designed to specifically recognize MAR and PAR (37, 38). The use of these antibodies should enhance the feasibility of this assay for many labs that are not equipped for radioactive work. Utilizing these antibodies, we further developed an ELISA assay for de-MARylation that has the ability to dramatically increase the number of samples that can be analyzed compared to the gel-based assay. To our knowledge, previously developed ELISA assays were to measure the ADP-ribosyltransferase activities (39) but no ELISA has been established to test the ADP-ribosylhydrolase activity of macrodomain proteins. This ELISA assay should be useful to those in the field for defining enzyme kinetics and screening compounds for macrodomain inhibitors that could be either valuable research tools or potential therapeutics.

bioRxiv preprint doi: https://doi.org/10.1101/2020.05.11.089375; this version posted June 1, 2020. The copyright holder for this preprint (which was not certified by peer review) is the author/funder. All rights reserved. No reuse allowed without permission.

The functional importance of Mac1 has been demonstrated in several reports, mostly utilizing the mutation of a highly conserved asparagine that mediates contact with the distal ribose (Fig. 3B) (16, 19, 20). However, the proteins that are targeted by the CoV Mac1 for de-ADP-ribosylation remains unknown. Regardless, from these reports it is clear that CoV Mac1 is vital for the ability of these viruses to cause disease, and have indicated that it could be a novel therapeutic target. Despite this, there are no known compounds that inhibit this domain. The outbreak of COVID-19 has illustrated an incredible need for developing multiple therapeutic drugs targeting conserved coronavirus proteins. Mac1 appears to be an ideal candidate for further drug development based on its: *i)* highly conserved structure and biochemical activities within CoVs; and *ii)* clear importance for multiple CoVs to cause disease. Targeting Mac1 may also have the benefit of enhancing the innate immune response, as we have shown that Mac1 is required for some CoVs to block IFN production (16, 21). Considering that Mac1 proteins from divergent αCoVs such as 229E and FIPV also have de-ADP-ribosylating activity (14, 15), it is possible that compounds targeting Mac1 could prevent disease caused by of wide variety of CoV, including those of veterinary importance like porcine epidemic diarrhea virus (PEDV). Additionally, compounds that inhibit Mac1 in combination with the structure could help identify the mechanisms it uses to bind to its biologically relevant protein substrates, remove ADP-ribose from these proteins, and potentially define the precise function for Mac1 in SARS-CoV-2 replication and pathogenesis. In conclusion, the results described here will be critical for the design and development of highly-specific Mac1 inhibitors that could be used therapeutically to mitigate COVID-19 or future CoV outbreaks.

bioRxiv preprint doi: https://doi.org/10.1101/2020.05.11.089375; this version posted June 1, 2020. The copyright holder for this preprint (which was not certified by peer review) is the author/funder. All rights reserved. No reuse allowed without permission.

METHODS

Plasmids

The SARS-CoV macrodomain (Mac1) (residues 1000-1172 of pp1a) was cloned into the pET21a+ expression vector with an N-terminal His tag. The MERS-CoV Mac1 (residues 1110-1273 of pp1a) was also cloned into pET21a+ with a C-terminal His tag. SARS-CoV-2 Mac1 (residues 1023-1197 of pp1a) was cloned into the pET30a+ expression vector with an N-terminal His tag and a TEV cleavage site (Synbio). The pETM-CN Mdo2 Mac1 (residues 7-243) expression vector with an N-terminal His-TEV-V5 tag and the pGEX4T-PARP10-CD (residues 818-1025) expression vector with an N-terminal GST tag were previously described (30). All plasmids were confirmed by restriction digest, PCR, and direct sequencing.

Protein Expression and Purification

A single colony of *E. coli* cells (C41(DE3)) containing plasmids harboring the constructs of the macrodomain proteins was inoculated into 10 mL LB media and grown overnight at 37°C with shaking at 250 rpm. The overnight culture was transferred to a shaker flask containing 2X 1L TB media at 37°C until the OD600 reached 0.7. The proteins were either induced with 0.4 mM IPTG at 37°C for 3 hours, or 17°C for 20 hours. Cells were pelleted at 3500 × g for 10 min and frozen at -80°C. Frozen cells were thawed at room temperature, resuspended in 50 mM Tris (pH 7.6), 150 mM NaCl, and sonicated using the following cycle parameters: Amplitude: 50%, Pulse length: 30 seconds, Number of pulses: 12, while incubating on ice for >1min between pulses. The soluble fraction was obtained by centrifuging the cell lysate at 45,450 × g for 30 minutes at 4°C. The expressed soluble proteins were purified by affinity chromatography using a 5 ml prepacked HisTrap HP column on an AKTA Pure protein purification system (GE Healthcare). The fractions were further purified by size-exclusion chromatography (SEC) with a

bioRxiv preprint doi: https://doi.org/10.1101/2020.05.11.089375; this version posted June 1, 2020. The copyright holder for this preprint (which was not certified by peer review) is the author/funder. All rights reserved. No reuse allowed without permission.

Superdex 75 10/300 GL column equilibrated with 20mM Tris (pH 8.0), 150 mM NaCl and the protein sized as a monomer relative to the column calibration standards. To cleave off the His tag from the SARS-CoV-2 Mac1, purified TEV protease was added to purified SARS-CoV-2 Mac1 protein at a ratio of 1:10 (w/w), and then passed back through the Ni-NTA HP column. Protein was collected in the flow through and equilibrated with 20 mM Tris (pH 8.0), 150 mM NaCl. The SARS-CoV-2 Mac1, free from the N-terminal 6X-His tag, was used for subsequent crystallization experiments.

For the PARP10-CD protein, the cell pellet was resuspended in 50 mM Tris-HCl (pH 8.0), 500 mM NaCl, 0.1mM EDTA, 25% glycerol, 1 mM DTT and sonicated as described above. The cell lysate was incubated with 10 ml of Glutathione Sepharose 4B resin from GE Healthcare, equilibrated with the same buffer for 2 hours, then applied to a gravity flow column to allow unbound proteins to flow through. The column was washed with the resuspension buffer till the absorbance at 280 nm reached baseline. The bound protein was eluted out of the column with resuspension buffer containing 20 mM reduced glutathione and then dialyzed back into the resuspension buffer overnight at 4°C.

Isothermal Titration Calorimetry

All ITC titrations were performed on a MicroCal PEAQ-ITC instrument (Malvern Pananalytical Inc., MA). All reactions were performed in 20 mM Tris pH 7.5, 150 mM NaCl using 100 μM of all macrodomain proteins at 25°C. Titration of 2 mM ADP-ribose or ATP (MilliporeSigma) contained in the stirring syringe included a single 0.4 μL injection, followed by 18 consecutive injections of 2 μL. Data analysis of thermograms was analyzed using one set of binding sites model of the MicroCal ITC software to obtain all fitting model parameters for the experiments.

bioRxiv preprint doi: https://doi.org/10.1101/2020.05.11.089375; this version posted June 1, 2020. The copyright holder for this preprint (which was not certified by peer review) is the author/funder. All rights reserved. No reuse allowed without permission.

Differential Scanning Fluorimetry (DSF)

Thermal shift assay with DSF involved use of LightCycler® 480 Instrument (Roche Diagnostics). In total, a 15 µL mixture containing 8X SYPRO Orange (Invitrogen), and 10 µM macrodomain protein in buffer containing 20 mM Hepes, NaOH, pH 7.5 and various concentrations of ADP-ribose were mixed on ice in 384-well PCR plate (Roche). Fluorescent signals were measured from 25 to 95 °C in 0.2 °C/30-s steps (excitation, 470-505 nm; detection, 540-700 nm). The main measurements were carried out in triplicate. Data evaluation and Tm determination involved use of the Roche LightCycler® 480 Protein Melting Analysis software, and data fitting calculations involved the use of single site binding curve analysis on Graphpad Prism.

De-MARylation Assays

Automodification of PARP10-CD protein: A 10 µM solution of purified PAPR10-CD protein was incubated for 20 minutes at 37°C with 1 mM final concentration of β-Nicotinamide Adenine Dinucleotide (β NAD^+) (Millipore-Sigma) in a reaction buffer (50 mM HEPES, 150 mM NaCl, 0.2 mM DTT, and 0.02% NP-40). MARylated PARP10 was aliquoted and stored at -80°C.

PAPR10-CD ADP-ribose hydrolysis: All reactions were performed at 37°C for the designated time. A 1 µM solution of MARylated PARP10-CD and purified Mac1 protein was added in the reaction buffer (50 mM HEPES, 150 mM NaCl, 0.2 mM DTT, and 0.02% NP-40). The reaction was stopped with addition of 2X Laemmli sample buffer containing 10% β-mercaptoethanol.

Protein samples were heated at 95°C for 5 minutes before loading and separated onto SDS-PAGE cassette (Thermo Fisher Scientific Bolt™ 4-12% Bis-Tris Plus Gels) in MES

bioRxiv preprint doi: https://doi.org/10.1101/2020.05.11.089375; this version posted June 1, 2020. The copyright holder for this preprint (which was not certified by peer review) is the author/funder. All rights reserved. No reuse allowed without permission.

running buffer. For direct protein detection, the SDS-PAGE gel was stained using InstantBlue® Protein Stain (Expedeon). For immunoblotting, the separated proteins were transferred onto polyvinylidene difluoride (PVDF) membrane using iBlot™ 2 Dry Blotting System (ThermoFisher Scientific). The blot was blocked with 5% skim milk in PBS containing 0.05% Tween-20 and probed with anti-mono or poly ADP-ribose binding antibodies MABE1076 (α-MAR), MABC547 (α-PAR), MABE1075 (α-MAR/PAR) (Millipore-Sigma) and anti-GST tag monoclonal antibody MA4-004 (ThermoFisher Scientific). The primary antibodies were detected with secondary infrared anti-rabbit and anti-mouse antibodies (LI-COR Biosciences). All immunoblots were visualized using Odyssey® CLx Imaging System (LI-COR Biosciences). The images were quantitated using Image J software (National Institutes for Health (NIH)).

ELISA-based MAR hydrolysis: ELISA Well-Coated™ Glutathione plates (G-Biosciences, USA) were washed with phosphate-buffered saline (PBS) containing 0.05% Tween-20 (PBS-T) and incubated with 50 µL of 100 nM automodified MARylated PARP10-CD in PBS for one hour under room temperature. Following four washes with PBS-T, variable concentrations of SARS-CoV-2 Mac1 were incubated with MARylated PARP10-CD for 30 minutes at 37°C. Purified macrodomains were 2-fold serially diluted starting at 100 nM in reaction buffer prior to addition to MARylated PARP10-CD. Subsequently, ELISA wells were washed four times with PBS-T and incubated with 50 µL/well of anti-GST (Invitrogen MA4-004) or anti-MAR (Millipore-Sigma MAB1076) diluted 1:5,000 in 5 mg/ml BSA in PBS-T (BSA5-PBS-T) for 1 hour at room temperature. After four additional washes with PBS-T, each well was incubated with 50 µL diluted 1:5,000 in BSA5-PBS-T of anti-rabbit-HRP (SouthernBiotech, USA) or anti-mouse-HRP (Rockland Immunochemicals, USA) conjugate for 1 hour at room temperature. The plate was washed four times with PBS-T and 100 µL of TMB peroxidase substrate solution

bioRxiv preprint doi: https://doi.org/10.1101/2020.05.11.089375; this version posted June 1, 2020. The copyright holder for this preprint (which was not certified by peer review) is the author/funder. All rights reserved. No reuse allowed without permission.

(SouthernBiotech, USA) was added to each well and incubated for 10 minutes. The peroxidase reaction was stopped with 50 µL per well of 1 M HCl before proceeding to reading. Absorbance was measured at 450 nm and subtracted from 620 nm using Biotek Powerwave XS plate reader (BioTek). As controls, MARylated PARP10-CD and non-MARylated PARP10 were detected with both anti-MAR and anti-GST antibodies. The absorbance of non-MARylated PARP10-CD detected with anti-MAR antibody was used to establish the background signal. The % signal remaining was calculated by dividing the experimental signal (+ enzyme) minus background by the control (no enzyme) minus the background.

PAR Binding Assay

Proteins were slot-blotted on a 0.2 µm pore–size nitrocellulose membrane (Bio-Rad) using a Bio-Dot® microfiltration apparatus (Bio-Rad). Sixty picomoles of macrodomain proteins Mdo2, SARS-CoV, MERS-CoV and SARS-CoV-2 diluted in 200 µL TBS (20 mM Tris-HCl pH 7.5, 150 mM NaCl) were applied to the vacuum manifold sample template. Calf thymus histone H1 (Calbiochem) and DNAse I (Roche) were respectively used as positive and negative PAR-binding proteins. Following complete aspiration of the protein samples, the nitrocellulose membrane was rinsed three times in 50 mL TBS-T (20 mM Tris-HCl pH 7.5, 150 mM NaCl, 0.01% Tween-20). The membrane was incubated with TBS-T containing 100 nM PAR purified by dihydroxyboronyl Bio-Rex (DHBB) chromatography (40). The membranes were extensively washed with TBS-T and blocked with a PBS-MT solution (PBS supplemented with 5% milk and 0.1% Tween-20) for 1 hour. The membrane was then incubated with the anti-PAR monoclonal antibody clone 10H (Tulip Biolabs) or the polyclonal antibody 96-10 (38) for 1 hour. The membrane was extensively washed with PBS-T and incubated with the corresponding peroxidase-conjugated secondary antibodies (Jackson ImmunoResearch) for 30 min. The

bioRxiv preprint doi: https://doi.org/10.1101/2020.05.11.089375; this version posted June 1, 2020. The copyright holder for this preprint (which was not certified by peer review) is the author/funder. All rights reserved. No reuse allowed without permission.

membrane was finally washed three times with PBS-T and signal was detected using the Western Lightning® Plus ECL chemiluminescence substrate (PerkinElmer). SYPRO™ Ruby protein blot stain was used according to the manufacturer's protocol (Bio-Rad) to assess the efficiency of protein transfer to the nitrocellulose membrane. Fluorescence imaging was acquired using a Geliance CCD-based bioimaging system (PerkinElmer).

De-PARylation Assay

Automodification of PARP1 protein: PARP1 was incubated with increasing concentrations of NAD^+ to generate a range of PARP1 automodification levels. Highly purified human 6X-His-PARP1 (41) (5 µg) was incubated for 30 min at 30°C in a reaction buffer containing 100 mM Tris-HCl pH 8.0, 10 mM $MgCl_2$, 10% (v/v) glycerol, 10 mM DTT, 0 to 500 µM NAD+, 10% (v/v) ethanol and 25 µg/mL calf thymus activated DNA (Sigma-Aldrich).

PARP1 ADP-ribose hydrolysis: To evaluate the PAR hydrolase activity of CoV macrodomains, 200 ng of slightly automodified PARP1 with 5 µM NAD^+ or highly automodified with 500 µM NAD^+ were used as substrates for the de-PARylation assays. Recombinant macrodomain protein (1 µg) was supplemented to the reaction buffer (100 mM Tris-HCl pH 8.0, 10% (v/v) glycerol and 10 mM DTT) containing automodified PARP1 and incubated for 1 hour at 37°C. Recombinant PARG (1 µg) was used as a positive control for PAR erasing (42). Reaction mixtures were resolved on 4–12% Criterion™ XT Bis-Tris protein gels, transferred onto nitrocellulose membrane and probed with the anti-PAR polyclonal antibody 96-10 as described for the polymer-blot assays.

Structure Determination

Crystallization and Data Collection: Purified SARS-CoV-2 Mac1 in 150 mM NaCl, 20 mM Tris pH 8.0 was concentrated to 13.8 mg/mL for crystallization screening. All crystallization

bioRxiv preprint doi: https://doi.org/10.1101/2020.05.11.089375; this version posted June 1, 2020. The copyright holder for this preprint (which was not certified by peer review) is the author/funder. All rights reserved. No reuse allowed without permission.

492 experiments were setup using an NT8 drop-setting robot (Formulatrix Inc.) and UVXPO MRC
493 (Molecular Dimensions) sitting drop vapor diffusion plates at 18°C. 100 nL of protein and 100
494 nL crystallization solution were dispensed and equilibrated against 50 µL of the latter. The
495 SARS-CoV-2 Mac1 complex with ADP-ribose was prepared by adding the ligand, from a 100
496 mM stock in water, to the protein at a final concentration of 2 mM. Crystals that were obtained in
497 1-2 days from the Salt Rx HT screen (Hampton Research) condition E10 (1.8 M
498 NaH_2PO_4/K_2HPO_4, pH 8.2). Refinement screening was conducted using the additive screen HT
499 (Hampton Research) by supplementing 10% of each additive to the Salt Rx HT E10 condition in
500 a new 96-well UVXPO crystallization plate. The crystals used for data collection were obtained
501 from Salt Rx HT E10 supplemented with 0.1 M NDSB-256 from the additive screen (Fig. S1).
502 Samples were transferred to a fresh drop composed of 80% crystallization solution and 20%
503 (v/v) PEG 200 and stored in liquid nitrogen. X-ray diffraction data were collected at the
504 Advanced Photon Source, IMCA-CAT beamline 17-ID using a Dectris Eiger 2X 9M pixel array
505 detector.

506 *Structure Solution and Refinement*: Intensities were integrated using XDS (43, 44) via
507 Autoproc (45) and the Laue class analysis and data scaling were performed with Aimless (46).
508 Notably, a pseudo-translational symmetry peak was observed at (0, 0.31 0.5) that was 44.6% of
509 the origin. Structure solution was conducted by molecular replacement with Phaser (47) using a
510 previously determined structure of ADP-ribose bound SARS-CoV-2 Mac1 (PDB 6W02) as the
511 search model. The top solution was obtained in the space group $P2_1$ with four molecules in the
512 asymmetric unit. Structure refinement and manual model building were conducted with Phenix
513 (48) and Coot (49) respectively. Disordered side chains were truncated to the point for which
514 electron density could be observed. Structure validation was conducted with Molprobity (50) and

bioRxiv preprint doi: https://doi.org/10.1101/2020.05.11.089375; this version posted June 1, 2020. The copyright holder for this preprint (which was not certified by peer review) is the author/funder. All rights reserved. No reuse allowed without permission.

figures were prepared using the CCP4MG package (51). Superposition of the macrodomain structures was conducted with GESAMT (52).

Statistical Analysis

All statistical analyses were done using an unpaired two-tailed student's t-test to assess differences in mean values between groups, and graphs are expressed as mean ±SD. Significant p values are denoted with *$p \leq 0.05$.

ACCESSION CODES

The coordinates and structure factors for SARS-CoV-2 Mac1 were deposited to the Worldwide Protein Databank (wwPDB) with the accession code 6WOJ.

ACKNOWLEDGEMENTS

We'd like to thank Ivan Ahel and Gytis Jankevicius (Oxford University) for providing protein expression plasmids; John Pascal (University of Montreal) and Marie-France Langelier (Universite de Montreal) for providing PARP1; and Wenqing Xu (University of Washington) for providing PARG. This research was funded by the National Institutes of Health (NIH), grant numbers P20 GM113117, P30GM110761, and AI134993-01 to A.R.F and the Canadian Institutes of Health Research, grant number MOP-418863 to G.G.P. Use of the IMCA-CAT beamline 17-ID at the Advanced Photon Source was supported by the companies of the Industrial Macromolecular Crystallography Association through a contract with Hauptman-Woodward Medical Research Institute. Use of the Advanced Photon Source was supported by the U.S. Department of Energy, Office of Science, Office of Basic Energy Sciences, under Contract No. DE-AC02-06CH11357.

bioRxiv preprint doi: https://doi.org/10.1101/2020.05.11.089375; this version posted June 1, 2020. The copyright holder for this preprint (which was not certified by peer review) is the author/funder. All rights reserved. No reuse allowed without permission.

AUTHOR CONTRIBUTIONS

Conceptualization: ARF, YMOA, GGP

Data curation: YMOA, SL, ARF

Formal analysis: YMOA, DKJ, AR, SL, ARF

Funding acquisition: GGP, SL, ARF

Investigation: YMOA, MMK, AR, JPG, LN, PM, KPB

Methodology: YMOA, GGP, AR, JPG, SL, ARF

Project administration: GGP, SL, ARF

Resources: PG, ARF

Supervision: GGP, SL ARF

Validation: YMOA, SL, AR, JPG, GGP, ARF

Visualization: YMOA, ARF, AR, SL, JPG

Writing – original draft: YMOA, SL, ARF

Writing – review & editing: all authors

bioRxiv preprint doi: https://doi.org/10.1101/2020.05.11.089375; this version posted June 1, 2020. The copyright holder for this preprint (which was not certified by peer review) is the author/funder. All rights reserved. No reuse allowed without permission.

552 **REFERENCES**
553
554 1. Zhou P, Yang XL, Wang XG, Hu B, Zhang L, Zhang W, Si HR, Zhu Y, Li B, Huang CL,
555 Chen HD, Chen J, Luo Y, Guo H, Jiang RD, Liu MQ, Chen Y, Shen XR, Wang X, Zheng
556 XS, Zhao K, Chen QJ, Deng F, Liu LL, Yan B, Zhan FX, Wang YY, Xiao GF, Shi ZL.
557 2020. A pneumonia outbreak associated with a new coronavirus of probable bat origin.
558 Nature 579:270-273.
559 2. Coronaviridae Study Group of the International Committee on Taxonomy of V. 2020.
560 The species Severe acute respiratory syndrome-related coronavirus: classifying 2019-
561 nCoV and naming it SARS-CoV-2. Nat Microbiol 5:536-544.
562 3. Srinivasan S, Cui H, Gao Z, Liu M, Lu S, Mkandawire W, Narykov O, Sun M, Korkin D.
563 2020. Structural Genomics of SARS-CoV-2 Indicates Evolutionary Conserved
564 Functional Regions of Viral Proteins. Viruses 12:360.
565 4. Wu C, Liu Y, Yang Y, Zhang P, Zhong W, Wang Y, Wang Q, Xu Y, Li M, Li X, Zheng
566 M, Chen L, Li H. 2020. Analysis of therapeutic targets for SARS-CoV-2 and discovery
567 of potential drugs by computational methods. Acta Pharm Sin B
568 doi:10.1016/j.apsb.2020.02.008.
569 5. Fehr AR, Perlman S. 2015. Coronaviruses: An Overview of Their Replication and
570 Pathogenesis, p 1-23. *In* Maier HJ, Bickerton E, Britton P (ed), Coronaviruses, vol 1282.
571 Springer New York.
572 6. Egloff MP, Malet H, Putics A, Heinonen M, Dutartre H, Frangeul A, Gruez A,
573 Campanacci V, Cambillau C, Ziebuhr J, Ahola T, Canard B. 2006. Structural and
574 functional basis for ADP-ribose and poly(ADP-ribose) binding by viral macro domains. J
575 Virol 80:8493-502.
576 7. Putics A, Filipowicz W, Hall J, Gorbalenya AE, Ziebuhr J. 2005. ADP-ribose-1"-
577 monophosphatase: a conserved coronavirus enzyme that is dispensable for viral
578 replication in tissue culture. J Virol 79:12721-31.
579 8. Saikatendu KS, Joseph JS, Subramanian V, Clayton T, Griffith M, Moy K, Velasquez J,
580 Neuman BW, Buchmeier MJ, Stevens RC, Kuhn P. 2005. Structural basis of severe acute
581 respiratory syndrome coronavirus ADP-ribose-1"-phosphate dephosphorylation by a
582 conserved domain of nsP3. Structure 13:1665-75.
583 9. Cho CC, Lin MH, Chuang CY, Hsu CH. 2016. Macro Domain from Middle East
584 Respiratory Syndrome Coronavirus (MERS-CoV) Is an Efficient ADP-ribose Binding
585 Module: CRYSTAL STRUCTURE AND BIOCHEMICAL STUDIES. J Biol Chem
586 291:4894-902.
587 10. Xu YY, Cong L, Chen C, Wei L, Zhao Q, Xu XL, Ma YL, Bartlam M, Rao ZH. 2009.
588 Crystal Structures of Two Coronavirus ADP-Ribose-1 "-Monophosphatases and Their
589 Complexes with ADP-Ribose: a Systematic Structural Analysis of the Viral ADRP
590 Domain. Journal of Virology 83:1083-1092.
591 11. Makrynitsa GI, Ntonti D, Marousis KD, Birkou M, Matsoukas MT, Asami S, Bentrop D,
592 Papageorgiou N, Canard B, Coutard B, Spyroulias GA. 2019. Conformational plasticity
593 of the VEEV macro domain is important for binding of ADP-ribose. J Struct Biol
594 206:119-127.
595 12. Malet H, Coutard B, Jamal S, Dutartre H, Papageorgiou N, Neuvonen M, Ahola T,
596 Forrester N, Gould EA, Lafitte D, Ferron F, Lescar J, Gorbalenya AE, de Lamballerie X,
597 Canard B. 2009. The crystal structures of Chikungunya and Venezuelan equine

bioRxiv preprint doi: https://doi.org/10.1101/2020.05.11.089375; this version posted June 1, 2020. The copyright holder for this preprint (which was not certified by peer review) is the author/funder. All rights reserved. No reuse allowed without permission.

598 encephalitis virus nsP3 macro domains define a conserved adenosine binding pocket. J
599 Virol 83:6534-45.
600 13. Rack JG, Perina D, Ahel I. 2016. Macrodomains: Structure, Function, Evolution, and
601 Catalytic Activities. Annu Rev Biochem 85:431-54.
602 14. Li C, Debing Y, Jankevicius G, Neyts J, Ahel I, Coutard B, Canard B. 2016. Viral Macro
603 Domains Reverse Protein ADP-Ribosylation. J Virol 90:8478-86.
604 15. Eckei L, Krieg S, Butepage M, Lehmann A, Gross A, Lippok B, Grimm AR, Kummerer
605 BM, Rossetti G, Luscher B, Verheugd P. 2017. The conserved macrodomains of the non-
606 structural proteins of Chikungunya virus and other pathogenic positive strand RNA
607 viruses function as mono-ADP-ribosylhydrolases. Sci Rep 7:41746.
608 16. Fehr AR, Channappanavar R, Jankevicius G, Fett C, Zhao J, Athmer J, Meyerholz DK,
609 Ahel I, Perlman S. 2016. The Conserved Coronavirus Macrodomain Promotes Virulence
610 and Suppresses the Innate Immune Response during Severe Acute Respiratory Syndrome
611 Coronavirus Infection. mBio 7:e01721-16.
612 17. Kim DS, Challa S, Jones A, Kraus WL. 2020. PARPs and ADP-ribosylation in RNA
613 biology: from RNA expression and processing to protein translation and proteostasis.
614 Genes Dev 34:302-320.
615 18. Fehr AR, Singh SA, Kerr CM, Mukai S, Higashi H, Aikawa M. 2020. The impact of
616 PARPs and ADP-ribosylation on inflammation and host-pathogen interactions. Genes
617 Dev 34:341-359.
618 19. Eriksson KK, Cervantes-Barragan L, Ludewig B, Thiel V. 2008. Mouse hepatitis virus
619 liver pathology is dependent on ADP-ribose-1"-phosphatase, a viral function conserved in
620 the alpha-like supergroup. J Virol 82:12325-34.
621 20. Fehr AR, Athmer J, Channappanavar R, Phillips JM, Meyerholz DK, Perlman S. 2015.
622 The nsp3 macrodomain promotes virulence in mice with coronavirus-induced
623 encephalitis. J Virol 89:1523-36.
624 21. Grunewald ME, Chen Y, Kuny C, Maejima T, Lease R, Ferraris D, Aikawa M, Sullivan
625 CS, Perlman S, Fehr AR. 2019. The coronavirus macrodomain is required to prevent
626 PARP-mediated inhibition of virus replication and enhancement of IFN expression. PLoS
627 Pathog 15:e1007756.
628 22. Alhammad YMO, Fehr AR. 2020. The Viral Macrodomain Counters Host Antiviral
629 ADP-Ribosylation. Viruses 12:384.
630 23. Abraham R, Hauer D, McPherson RL, Utt A, Kirby IT, Cohen MS, Merits A, Leung
631 AKL, Griffin DE. 2018. ADP-ribosyl-binding and hydrolase activities of the alphavirus
632 nsP3 macrodomain are critical for initiation of virus replication. Proc Natl Acad Sci U S
633 A 115:E10457-E10466.
634 24. Abraham R, McPherson RL, Dasovich M, Badiee M, Leung AKL, Griffin DE. 2020.
635 Both ADP-Ribosyl-Binding and Hydrolase Activities of the Alphavirus nsP3
636 Macrodomain Affect Neurovirulence in Mice. mBio 11.
637 25. McPherson RL, Abraham R, Sreekumar E, Ong SE, Cheng SJ, Baxter VK, Kistemaker
638 HA, Filippov DV, Griffin DE, Leung AK. 2017. ADP-ribosylhydrolase activity of
639 Chikungunya virus macrodomain is critical for virus replication and virulence. Proc Natl
640 Acad Sci U S A 114:1666-1671.
641 26. Parvez MK. 2015. The hepatitis E virus ORF1 'X-domain' residues form a putative
642 macrodomain protein/Appr-1"-pase catalytic-site, critical for viral RNA replication. Gene
643 566:47-53.

bioRxiv preprint doi: https://doi.org/10.1101/2020.05.11.089375; this version posted June 1, 2020. The copyright holder for this preprint (which was not certified by peer review) is the author/funder. All rights reserved. No reuse allowed without permission.

27. Vuksanovic N, Silvaggi, N.R. National Science Foundation (NSF, United States). 2020. High-resolution structure of the SARS-CoV-2 NSP3 Macro X domain doi: 10.2210/pdb6WEY/pdb. doi:10.2210/pdb6WEY/pdb.
28. Michalska K, Stols, L., Jedrzejczak, R., Endres, M., Babnigg, G., Kim, Y., Joachimiak, A., Center for Structural Genomics of Infectious Diseases (CSGID). 2020. Crystal Structure of ADP ribose phosphatase of NSP3 from SARS-CoV-2 in the apo doi: 10.2210/pdb6WEN/pdb. doi:10.2210/pdb6wen/pdb.
29. Michalska K, Kim, Y., Jedrzejczak, R., Maltseva, N., Endres, M., Mececar, A., Joachimiak, A., Center for Structural Genomics of Infectious Diseases (CSGID). 2020. Crystal Structure of ADP ribose phosphatase of NSP3 from SARS CoV-2 in the complex with ADP ribose doi: 10.2210/pdb6W02/pdb. doi:10.2210/pdb6W02/pdb.
30. Jankevicius G, Hassler M, Golia B, Rybin V, Zacharias M, Timinszky G, Ladurner AG. 2013. A family of macrodomain proteins reverses cellular mono-ADP-ribosylation. Nat Struct Mol Biol 20:508-14.
31. Lei J, Kusov Y, Hilgenfeld R. 2018. Nsp3 of coronaviruses: Structures and functions of a large multi-domain protein. Antiviral Res 149:58-74.
32. Malanga M, Althaus FR. 2011. Noncovalent protein interaction with poly (ADP-ribose), p 67-82, Poly (ADP-ribose) Polymerase. Springer.
33. Shull NP, Spinelli SL, Phizicky EM. 2005. A highly specific phosphatase that acts on ADP-ribose 1"-phosphate, a metabolite of tRNA splicing in Saccharomyces cerevisiae. Nucleic Acids Res 33:650-60.
34. Rosenthal F, Feijs KL, Frugier E, Bonalli M, Forst AH, Imhof R, Winkler HC, Fischer D, Caflisch A, Hassa PO, Luscher B, Hottiger MO. 2013. Macrodomain-containing proteins are new mono-ADP-ribosylhydrolases. Nat Struct Mol Biol 20:502-7.
35. Sharifi R, Morra R, Appel CD, Tallis M, Chioza B, Jankevicius G, Simpson MA, Matic I, Ozkan E, Golia B, Schellenberg MJ, Weston R, Williams JG, Rossi MN, Galehdari H, Krahn J, Wan A, Trembath RC, Crosby AH, Ahel D, Hay R, Ladurner AG, Timinszky G, Williams RS, Ahel I. 2013. Deficiency of terminal ADP-ribose protein glycohydrolase TARG1/C6orf130 in neurodegenerative disease. EMBO J 32:1225-37.
36. Ahel I, Ahel D, Matsusaka T, Clark AJ, Pines J, Boulton SJ, West SC. 2008. Poly(ADP-ribose)-binding zinc finger motifs in DNA repair/checkpoint proteins. Nature 451:81-5.
37. Gibson BA, Conrad LB, Huang D, Kraus WL. 2017. Generation and Characterization of Recombinant Antibody-like ADP-Ribose Binding Proteins. Biochemistry (Mosc) 56:6305-6316.
38. Affar EB, Duriez PJ, Shah RG, Winstall E, Germain M, Boucher C, Bourassa S, Kirkland JB, Poirier GG. 1999. Immunological determination and size characterization of poly(ADP-ribose) synthesized in vitro and in vivo. Biochim Biophys Acta 1428:137-46.
39. Asokanathan C, Tierney S, Ball CR, Buckle G, Day A, Tanley S, Bristow A, Markey K, Xing D, Yuen CT. 2018. An ELISA method to estimate the mono ADP-ribosyltransferase activities: e.g in pertussis toxin and vaccines. Anal Biochem 540-541:15-19.
40. Shah GM, Poirier D, Duchaine C, Brochu G, Desnoyers S, Lagueux J, Verreault A, Hoflack JC, Kirkland JB, Poirier GG. 1995. Methods for biochemical study of poly(ADP-ribose) metabolism in vitro and in vivo. Anal Biochem 227:1-13.

bioRxiv preprint doi: https://doi.org/10.1101/2020.05.11.089375; this version posted June 1, 2020. The copyright holder for this preprint (which was not certified by peer review) is the author/funder. All rights reserved. No reuse allowed without permission.

41. Langelier MF, Planck JL, Servent KM, Pascal JM. 2011. Purification of human PARP-1 and PARP-1 domains from Escherichia coli for structural and biochemical analysis. Methods Mol Biol 780:209-26.
42. Wang Z, Gagne JP, Poirier GG, Xu W. 2014. Crystallographic and biochemical analysis of the mouse poly(ADP-ribose) glycohydrolase. PLoS One 9:e86010.
43. Kabsch W. 1988. Evaluation of Single-Crystal X-Ray-Diffraction Data from a Position-Sensitive Detector. Journal of Applied Crystallography 21:916-924.
44. Kabsch W. 2010. Xds. Acta Crystallogr D Biol Crystallogr 66:125-32.
45. Vonrhein C, Flensburg C, Keller P, Sharff A, Smart O, Paciorek W, Womack T, Bricogne G. 2011. Data processing and analysis with the autoPROC toolbox. Acta Crystallogr D Biol Crystallogr 67:293-302.
46. Evans PR. 2011. An introduction to data reduction: space-group determination, scaling and intensity statistics. Acta Crystallogr D Biol Crystallogr 67:282-92.
47. McCoy AJ, Grosse-Kunstleve RW, Adams PD, Winn MD, Storoni LC, Read RJ. 2007. Phaser crystallographic software. J Appl Crystallogr 40:658-674.
48. Adams PD, Afonine PV, Bunkoczi G, Chen VB, Davis IW, Echols N, Headd JJ, Hung LW, Kapral GJ, Grosse-Kunstleve RW, McCoy AJ, Moriarty NW, Oeffner R, Read RJ, Richardson DC, Richardson JS, Terwilliger TC, Zwart PH. 2010. PHENIX: a comprehensive Python-based system for macromolecular structure solution. Acta Crystallogr D Biol Crystallogr 66:213-21.
49. Emsley P, Lohkamp B, Scott WG, Cowtan K. 2010. Features and development of Coot. Acta Crystallogr D Biol Crystallogr 66:486-501.
50. Chen VB, Arendall WB, 3rd, Headd JJ, Keedy DA, Immormino RM, Kapral GJ, Murray LW, Richardson JS, Richardson DC. 2010. MolProbity: all-atom structure validation for macromolecular crystallography. Acta Crystallogr D Biol Crystallogr 66:12-21.
51. Potterton L, McNicholas S, Krissinel E, Gruber J, Cowtan K, Emsley P, Murshudov GN, Cohen S, Perrakis A, Noble M. 2004. Developments in the CCP4 molecular-graphics project. Acta Crystallogr D Biol Crystallogr 60:2288-94.
52. Krissinel E. 2012. Enhanced fold recognition using efficient short fragment clustering. Journal of molecular biochemistry 1:76.
53. Evans P. 2006. Scaling and assessment of data quality. Acta Crystallogr D Biol Crystallogr 62:72-82.
54. Diederichs K, Karplus PA. 1997. Improved R-factors for diffraction data analysis in macromolecular crystallography. Nat Struct Biol 4:269-75.
55. Weiss MS. 2001. Global indicators of X-ray data quality. Journal of Applied Crystallography 34:130-135.
56. Evans P. 2012. Biochemistry. Resolving some old problems in protein crystallography. Science 336:986-7.
57. Karplus PA, Diederichs K. 2012. Linking crystallographic model and data quality. Science 336:1030-3.

bioRxiv preprint doi: https://doi.org/10.1101/2020.05.11.089375; this version posted June 1, 2020. The copyright holder for this preprint (which was not certified by peer review) is the author/funder. All rights reserved. No reuse allowed without permission.

730
731 **Table 1**. Crystallographic data for SARS-CoV-2 Mac1.
732

	SARS-CoV-2 Mac1
Data Collection	
Unit-cell parameters (Å, º)	*a*=59.72, *b*=83.17, *c*=84.24, *β*=94.4
Space group	$P2_1$
Resolution (Å)[1]	48.41-2.20 (2.27-2.20)
Wavelength (Å)	1.0000
Temperature (K)	100
Observed reflections	144,767
Unique reflections	41,586
$\langle I/\sigma(I)\rangle$[1]	7.3 (1.9)
Completeness (%)[1]	99.4 (99.7)
Multiplicity[1]	3.5 (3.4)
R_{merge} (%)[1,2]	13.0 (67.0)
R_{meas} (%)[1,4]	15.4 (79.2)
R_{pim} (%)[1,4]	8.2 (41.8)
$CC_{1/2}$ [1,5]	0.994 (0.849)
Refinement	
Resolution (Å)[1]	42.00-2.20
Reflections (working/test)[1]	39,474/1,966
R_{factor} / R_{free} (%)[1,3]	19.9/25.2
No. of atoms (Protein/Ligand/Water)	4,930/144/358
Model Quality	
R.m.s deviations	
Bond lengths (Å)	0.011
Bond angles (º)	1.144
Mean *B*-factor (Å)[2]	
All Atoms	28.1
Protein	27.9
Ligand	26.0
Water	30.9
Coordinate error (maximum likelihood) (Å)	0.31
Ramachandran Plot	
Most favored (%)	97.3
Additionally allowed (%)	2.4

733
734 1) Values in parenthesis are for the highest resolution shell.
735 2) $R_{merge} = \Sigma_{hkl}\Sigma_I |I_i(hkl) - \langle I(hkl)\rangle| / \Sigma_{hkl}\Sigma_I I_i(hkl)$, where $I_i(hkl)$ is the intensity
736 measured for the *i*th reflection and $\langle I(hkl)\rangle$ is the average intensity of all reflections with indices hkl.
737 3) $R_{factor} = \Sigma_{hkl} ||F_{obs}(hkl)| - |F_{calc}(hkl)|| / \Sigma_{hkl} |F_{obs}(hkl)|$; Rfree is calculated in an
738 identical manner using 5% of randomly selected reflections that were not included in the refinement.
739 4) R_{meas} = redundancy-independent (multiplicity-weighted) R_{merge} (46, 53). R_{pim} = precision-indicating (multiplicity-weighted) R_{merge} (54, 55)
740 5) $CC_{1/2}$ is the correlation coefficient of the mean intensities between two random half-sets of data (56, 57)

bioRxiv preprint doi: https://doi.org/10.1101/2020.05.11.089375; this version posted June 1, 2020. The copyright holder for this preprint (which was not certified by peer review) is the author/funder. All rights reserved. No reuse allowed without permission.

FIGURE LEGENDS

Figure 1. The SARS-CoV-2 Mac1 is a small domain within nsp3 and is highly conserved between other human CoV Mac1 protein domains. **(A)** Cartoon Schematic of the SARS-CoV-2 non-structural protein 3. The conserved macrodomain, or Mac1, is highlighted in yellow. **(B)** Sequence alignment of Mac1 from the highly-pathogenic human CoVs. Sequences were aligned using the ClustalW method from Clustal Omega online tool with manual adjustment. Identical residues are bolded, shaded in grey, and marked with asterisks.

Figure 2. Structure of SARS-CoV-2 Mac1 complexed with ADP-ribose. **A)** The structure was rendered as a blend through model from the N-terminus (blue) to the C-terminus (red). **B)** The structure was colored by secondary structure showing sheets (magenta) and helices (green). The ADP-ribose is rendered as gray cylinders with oxygens and nitrogens colored red and blue, respectively.

Figure 3. Binding mode of ADP-ribose in SARS-CoV-2 Mac1. **A)** Fo-Fc Polder omit map (green mesh) contoured at 3σ. **B)** Hydrogen bond interactions (dashed lines) between ADP-ribose and amino acids. **C)** Interactions with water molecules. Direct hydrogen bond interactions are represented by dashed lines and water mediated contacts to amino acids are drawn as solid lines.

Figure 4. Structural comparison of the SARS-CoV-2 Mac1 protein with the SARS-CoV and MERS-CoV Mac1 proteins. **A-B)** Superposition of SARS-CoV-2 macrodomain (magenta) with coronavirus macrodomain structures. **A**) SARS-CoV Mac1 with ADP-ribose (gold) (2FAV) and **B**) MERS-CoV Mac1 with ADP-ribose (teal) (5HOL). **C-D)** Superposition of SARS-CoV-2 Mac1 (magenta) with other coronavirus Mac1 structures highlighting the ADP-ribose binding site. **C**) SARS-CoV (gold), **D**) MERS-CoV (teal). The ADP-ribose molecules are colored gray

bioRxiv preprint doi: https://doi.org/10.1101/2020.05.11.089375; this version posted June 1, 2020. The copyright holder for this preprint (which was not certified by peer review) is the author/funder. All rights reserved. No reuse allowed without permission.

764 for SARS-CoV-2 Mac1 (**A-D**) and are rendered as green cylinders for SARS-CoV Mac1 (panel
765 **A,C**) and MERS-CoV Mac1 (panel **B,D**).

766 **Figure 5**. Human CoVs bind to ADP-ribose with similar affinity. **A-B)** ADP-ribose binding of
767 human Mdo2 and SARS-CoV, MERS-CoV, and SARS-CoV-2 Mac1 proteins by ITC. Images in
768 **(A)** are of one experiment representative of at least 2 independent experiments. Data in **(B)**
769 represent the combined averages of multiple independent experiments for each protein. Mdo2
770 n=2; SARS-CoV n=5; MERS-CoV n=6; SARS-CoV-2 n=2. **C)** PAR overlay assay of CoV
771 macrodomains. 60 pmoles of macrodomain proteins were slot-blotted on a nitrocellulose
772 membrane and probed with 100 nM purified PAR. PAR binding was detected with 10H and 96-
773 10 anti-PAR antibodies. Histone H1 (1 pmole) and DNAse I (60 pmoles) were used as positive
774 and negative PAR binding controls, respectively. Blots were stained with Sypro Ruby as a
775 loading control. The figure is representative of at least three independent experiments.

776 **Figure 6**. SARS-CoV-2, SARS-CoV, and MERS-CoV Mac1 proteins are potent ADP-
777 ribosylhydrolases. **A,C)** The SARS-CoV-2 macrodomain **(A)** or multiple macrodomain proteins
778 **(C)** were incubated with MARylated PARP10 CD *in vitro* for the indicated times at 37°C. ADP-
779 ribosylated PARP10 CD was detected by immunoblot (IB) with anti-mono ADP-ribose antibody
780 (Millipore-Sigma MAB1076). Total PARP10 CD and macrodomain protein levels were
781 determined by Coomassie Blue (CB) staining. PARP10 CD incubated alone at 37°C was stopped
782 at 0, 30 or 60 minutes. **B,D)** level of de-MARylation was measured by quantifying band intensity
783 using Image J software. Intensity values were plotted and fit to a non-linear regression curve **(B)**
784 or as bar graphs representing the means with error bars representing standard deviation **(D)**.
785 Results in **A** and **C** are representative experiments of two and three independent experiments,
786 respectively. Data in **B** and **D** represent the combined results of two and three independent

bioRxiv preprint doi: https://doi.org/10.1101/2020.05.11.089375; this version posted June 1, 2020. The copyright holder for this preprint (which was not certified by peer review) is the author/funder. All rights reserved. No reuse allowed without permission.

787 experiments, respectively. Asterisks indicate statistical significance between these samples at the
788 same timepoint from samples treated with Mdo2. **E)** PAR hydrolase assays were performed with
789 PARP1 either extensively poly-ADP-ribosylated (500 μM NAD^+) or partially poly-ADP-
790 ribosylated (5 μM NAD+) to produce oligo-ADP-ribose. Macrodomains were incubated with
791 both automodified PARP1 substrates for 1 hour. PAR was detected by Western blot with the
792 anti-PAR antibody 96-10. PARG (catalytically active 60 kD fragment) was used as a positive
793 control. The results are representative of at least 2 independent experiments.
794 **Figure 7.** Development of an ELISA assay to detect de-MARylation. **A)** Cartoon schematic of
795 the ELISA assay. ELISA plates pre-coated with glutathione and pre-blocked were used capture
796 GST-tagged PARP10 proteins, which was used as a substrate for de-MARylation. The removal
797 of MAR was detected by anti-MAR antibodies. **B)** MARylated PARP10 (MAR+) and non-
798 MARylated PARP10 (MAR-) with no SARS-CoV-2 Mac1 as controls were detected with anti-
799 mono ADP-ribose antibody α-MAR (Millipore-Sigma MAB1076) or with anti-GST α-GST
800 (Invitrogen, MA4-004). **C)** Starting at 100 nM, 2-fold serial dilutions of the SARS-CoV-2 Mac1
801 protein was incubated in individual wells with MARylated PARP10-CD for 30 min. at 37°C**.**
802 The graph represents the combined results of 3 independent experiments.
803

bioRxiv preprint doi: https://doi.org/10.1101/2020.05.11.089375; this version posted June 1, 2020. The copyright holder for this preprint (which was not certified by peer review) is the author/funder. All rights reserved. No reuse allowed without permission.

SUPPLEMENTAL FIGURE LEGENDS

Figure S1. Purification and crystallization of macrodomain proteins. **A)** Macrodomain proteins were purified as described in Methods. Equimolar amounts of the recombinant proteins were run on a polyacrylamide gel and visualized by Coomassie staining. **B)** Crystals of SARS-CoV-2 Mac1 obtained with Salt Rx HT E10 supplemented with 0.1 M NDSB-256.

Figure S2. Extended residues at the C-terminus of the SARS-CoV-2 Mac1 clashed with symmetry related molecules. **A)** Comparison of the amino acid sequence of SARS-CoV-2 Mac1, 6W02 and 6WEY. **B)** Superposition of SARS-CoV-2 Mac1 (magenta) subunit B onto subunit A of 6W02 reveals that the C-terminus would clash with symmetry related molecules (coral).

Figure S3. Comparison of the SARS-CoV-2 Mac1 protein with homologous structures. **A-B)** Superposition of SARS-CoV-2 Mac1 (magenta) with other recently determined homologous structures. **A)** SARS-CoV-2 Mac1 apo structure (6WEN), **B)** SARS-CoV-2 Mac1 complexed with ADP-ribose (6W02). The ADP-ribose molecule is colored gray for SARS-CoV-2 and is represented as green cylinders for 6W02 in panel **B**. **C-D)** Comparison of the residues in the ADP-ribose binding site. **C**) SARS-CoV-2 Mac1 apo structure (blue, 6WEN), **D**) SARS-CoV-2 Mac1 complexed with ADP-ribose (green, 6W02). The ADP-ribose of SARS-CoV-2 is rendered as gray cylinders, and is represented as green cylinders for 6W02 in panel **B**.

Figure S4. ADP-ribose binding of macrodomain proteins by DSF assay. 10 μM macrodomain protein was incubated with increasing concentrations of ADP-ribose and measured by DSF as described in Methods. Mdo2 n=4; SARS-CoV n=6; MERS-CoV n=5; SARS-CoV-2 n=3.

Figure S5. Affinity of ADP-ribose binding antibodies for ADP-ribosylated PARP10 CD. MARylated PARP10 and non-MARylated PARP10 CD were detected by immunoblot (IB) with anti-GST (Invitrogen, MA4-004), anti-ADP-ribose antibodies: anti-MAR (Millipore-Sigma

bioRxiv preprint doi: https://doi.org/10.1101/2020.05.11.089375; this version posted June 1, 2020. The copyright holder for this preprint (which was not certified by peer review) is the author/funder. All rights reserved. No reuse allowed without permission.

827 MAB1076), anti-PAR (Millipore-Sigma MABC547), and anti-MAR/PAR (Millipore-Sigma
828 MABE1075) antibodies.

829 **Figure S6**. Differential PARylation of PARP1 by varying concentrations of NAD^+. Recombinant
830 human PARP1 was automodified in a reaction buffer supplemented with increasing
831 concentration of NAD^+ to generate substrates for the PAR hydrolase assays. The presence of
832 PAR was detected by Western blot analysis of reaction products with the anti-PAR antibody 96-
833 10.

A

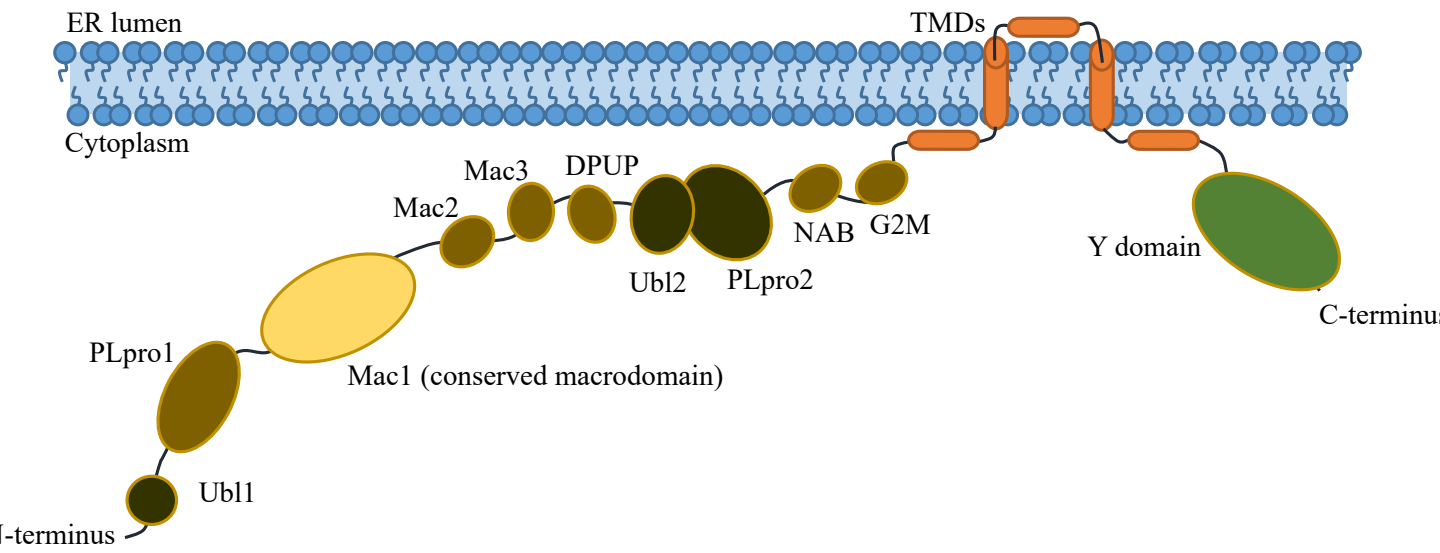

B

```
SARS-CoV-2 aa  1         10        20        30        40        50        58
               |         |         |         |         |         |         |
SARS-CoV-2     --IEVNSFSGYLKLTDNVYIKNADIVEEAKKVKPTVVVNAANVYLKHGGGVAGALNKATN 58
SARS-CoV       --EPVNQFTGYLKLTDNVAIKCVDIVKEAQSANPMVIVNAANIHLKHGGGVAGALNKATN 58
MERS-CoV       NVDPLSNFEHK-VITECVTIVLGDAIQVAKCYGESVLVNAANTHLKHGGGIAGAINAASK 59
                      *      *  * *   *    *       * *****  ****** *** * *

SARS-CoV-2 aa 60        70        80        90        100       110       118
               |         |         |         |         |         |         |
SARS-CoV-2     NAMQVESDDYIATNGPLKVGGSCVLSGHNLAKHCLHVVGPNVNKGEDIQLLKSAYEVFNQ 118
SARS-CoV       GAMQKESDDYIKLNGPLTVGGSCLLSGHNLAKKCLHVVGPNLNAGEDIQLLKAAYENFNS 118
MERS-CoV       GAVQKESDEYILAKGPLQVGDSVLLQGHSLAKNILHVVGPDARAKQDVSLLSKCYKAMNA 119
                * * *** **   *** ** *  * ** ***  ******      *  **   *   *

SARS-CoV-2 aa 120       130       140       150       160       170
               |         |         |         |         |         |
SARS-CoV-2     HEVLLAPLLSAGIFGADPIHSLRVCVDTVRTNVYLAVFDKNLYDKLVSSFLEMKSEK  175
SARS-CoV       QDILLAPLLSAGIFGAKPLQSLQVCVQTVRTQVYIAVNDKALYEQVVMDYLDNL-    172
MERS-CoV       YPLVVTPLVSAGIFGVKPAVSFDYLIREAKTRVLVVVNSQDVYKSLTIVDIPQLE    174
                     ** ******  *  *         * *   *     *
```

Figure 1. The SARS-CoV-2 Mac1 is a small domain within nsp3 and is highly conserved between other human CoV Mac1 protein domains. **(A)** Cartoon Schematic of the SARS-CoV-2 non-structural protein 3. The conserved macrodomain, or Mac1, is highlighted in yellow. **(B)** Sequence alignment of Mac1 from the highly-pathogenic human CoVs. Sequences were aligned using the ClustalW method from Clustal Omega online tool with manual adjustment. Identical residues are bolded, shaded in grey, and marked with asterisks.

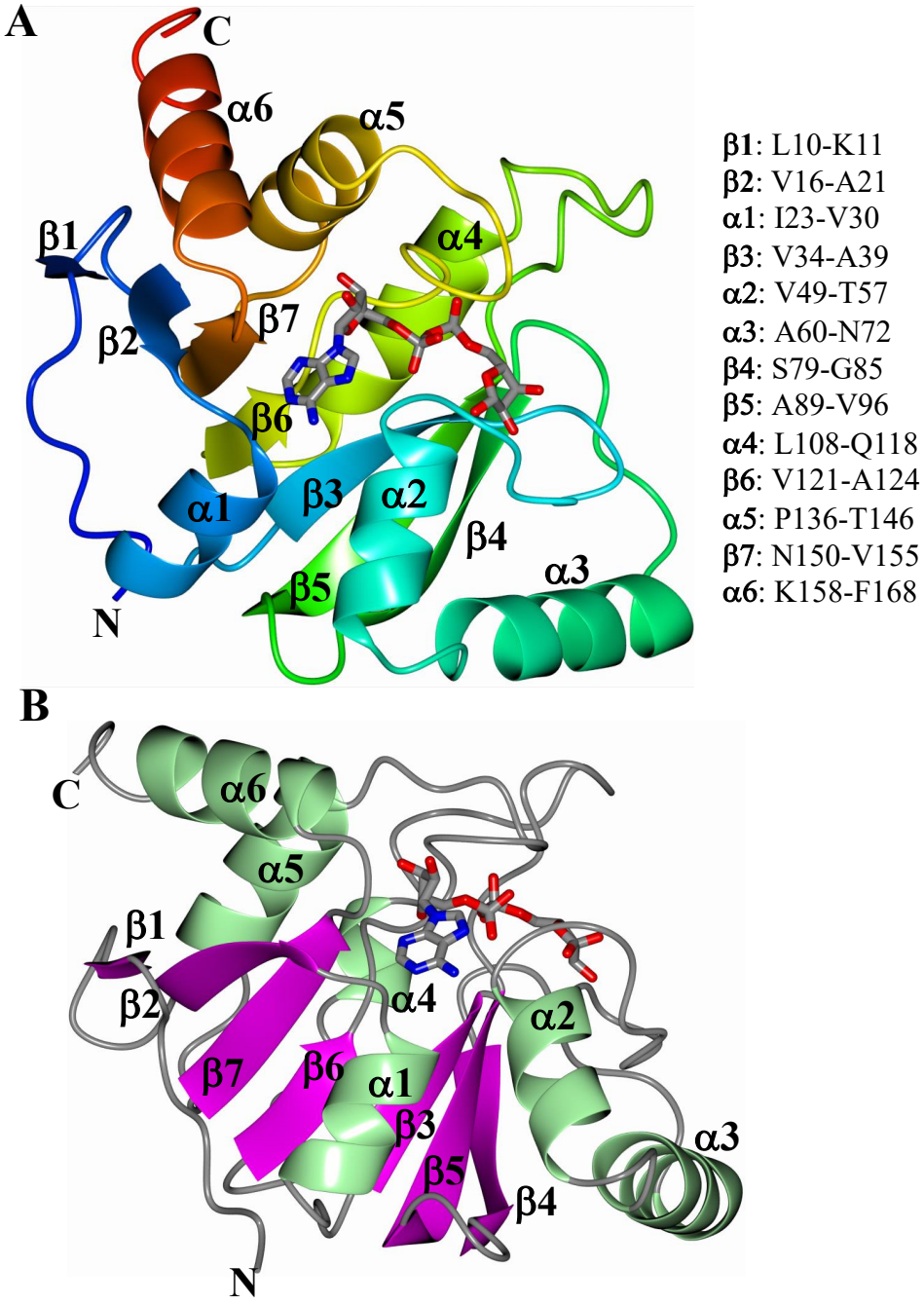

Figure 2. Structure of SARS-CoV-2 Mac1 complexed with ADP-ribose. **A)** The structure was rendered as a blend through model from the N-terminus (blue) to the C-terminus (red). **B)** The structure was colored by secondary structure showing sheets (magenta) and helices (green). The ADP-ribose is rendered as gray cylinders with oxygens and nitrogens colored red and blue, respectively.

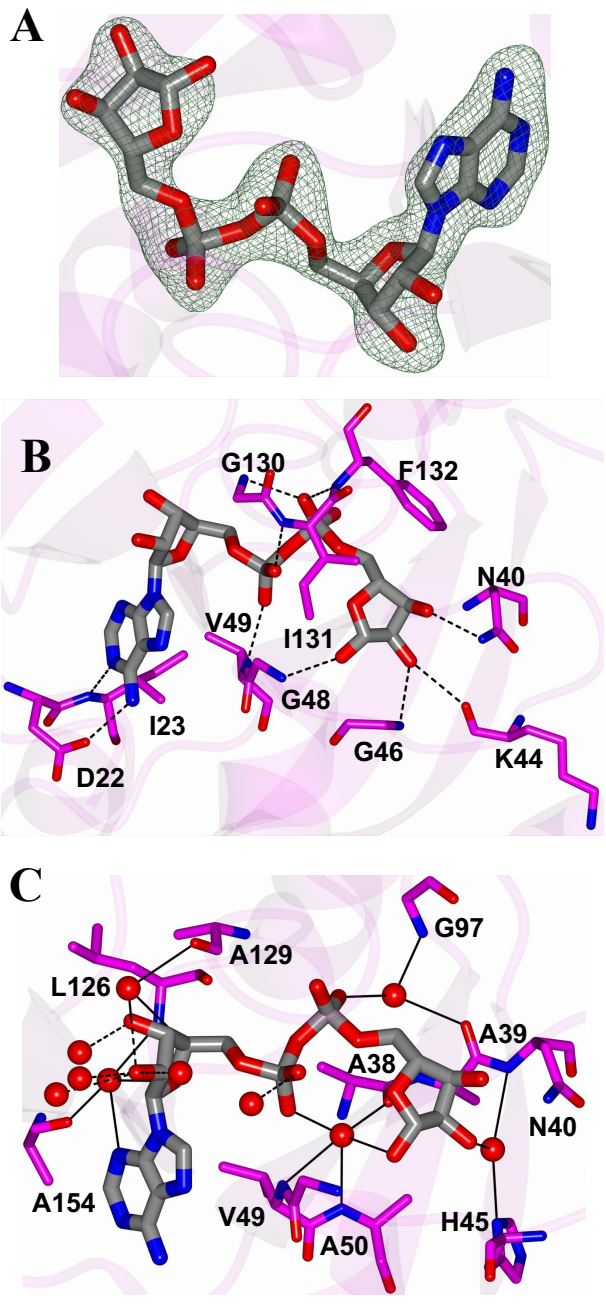

Figure 3. Binding mode of ADP-ribose in SARS-CoV-Mac1. **A)** Fo-Fc Polder omit map (green mesh) contoured at 3σ. **B)** Hydrogen bond interactions (dashed lines) between ADP-ribose and amino acids. **C)** Interactions with water molecules. Direct hydrogen bond interactions are represented by dashed lines and water mediated contacts to amino acids are drawn as solid lines.

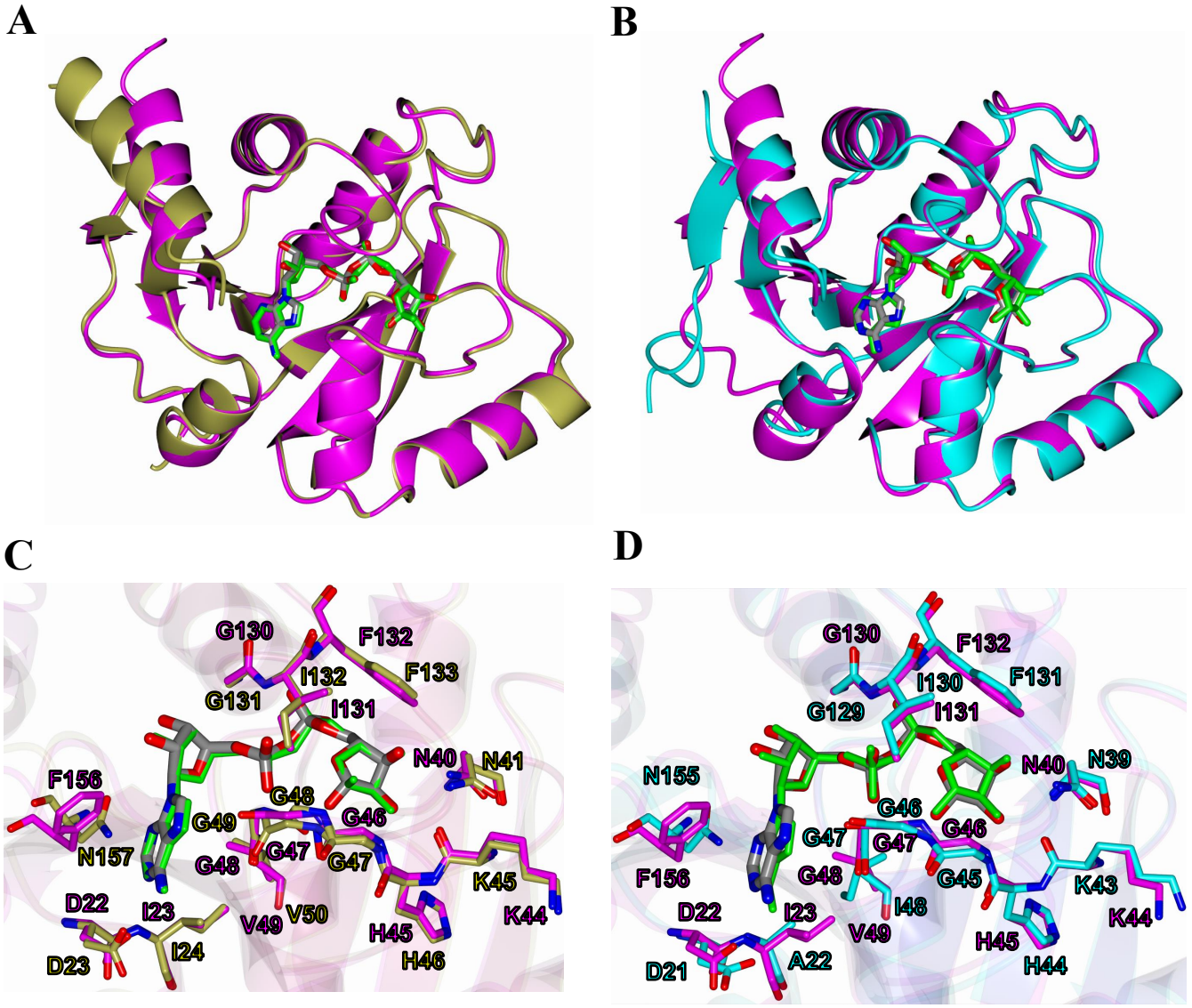

Figure 4. Superposition of SARS-CoV-2 macrodomain (magenta) with coronavirus macrodomain structures. **A**) SARS-CoV Mac1 with ADP-ribose (gold) (2FAV) and **B**) MERS-CoV Mac1 with ADP-ribose (teal) (5HOL). Superposition of SARS-CoV-2 Mac1 (magenta) with other coronavirus Mac1 structures highlighting the ADP-ribose binding site. **C**) SARS-CoV (gold), **D**) MERS-CoV (teal). The ADP-ribose molecules are colored gray for SARS-CoV-2 (A-D) and are rendered as green cylinders for SARS-CoV Mac1 (panel A,C) and MERS-CoV Mac1 (panel B,D).

A

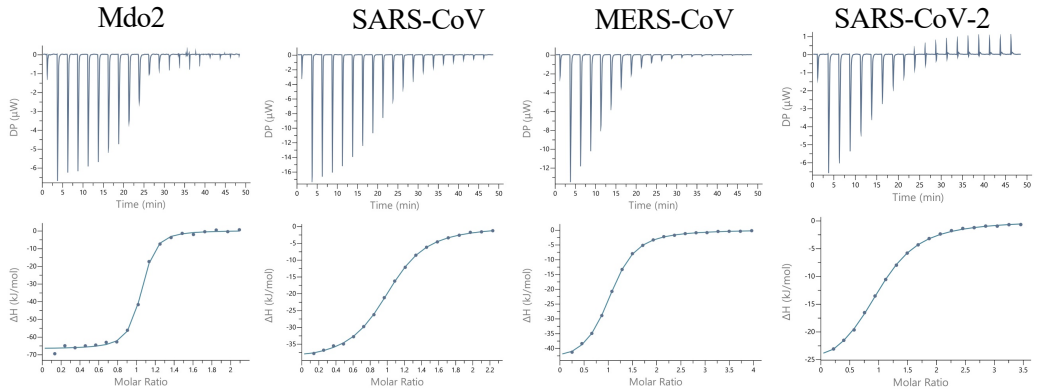

B

Macrodomain	Stoichiometry (N)	Kd (uM)	ΔH (kcal/mol)	ΔG (kcal/mol)
Mdo2	0.92 ± 0.01	0.24 ± 0.02	-66 ± 1	-38 ± 2
SARS-CoV	0.89 ± 0.04	10.8 ± 1.7	-40 ± 1.2	-28 ± 0.4
MERS-CoV	0.97 ± 0.04	7.9 ± 0.15	-47 ± 3	-29 ± 0.4
SARS-CoV-2	1.14 ± 0.06	16.8 ± 0.04	-28 ± 0.1	-27 ± 0.1

C

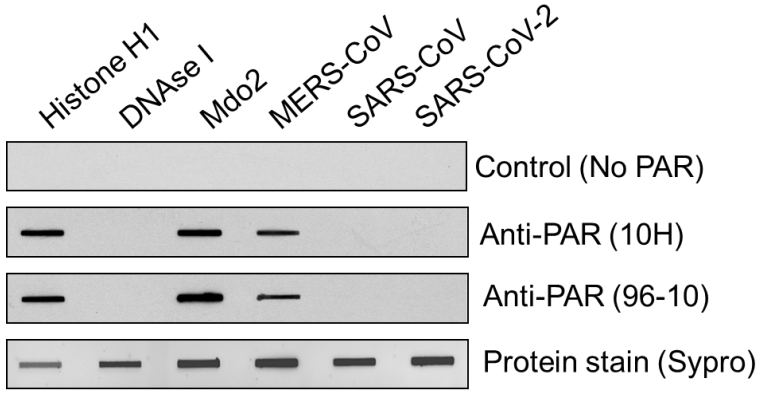

Figure 5. Human CoVs bind to ADP-ribose with similar affinity. **A-B)** ADP-ribose binding of human Mdo2 and SARS-CoV, MERS-CoV, and SARS-CoV-2 Mac1 proteins by ITC. Images in **(A)** are of one experiment representative of at least 2 independent experiments. Data in **(B)** represent the combined averages of multiple independent experiments for each protein. Mdo2 n=2; SARS-CoV n=5; MERS-CoV n=6; SARS-CoV-2 n=2. **C)** PAR overlay assay of CoV macrodomains. 60 pmoles of macrodomain proteins were slot-blotted on a nitrocellulose membrane and probed with 100 nM protein-free DHBB-purified PAR. PAR binding was detected with 10H and 96-10 anti-PAR antibodies. Histone H1 (1 pmole) and DNAse I (60 pmoles) were used as positive and negative PAR binding controls, respectively. Blots were stained with Sypro Ruby as a loading control. The figure is representative of at least three independent experiments.

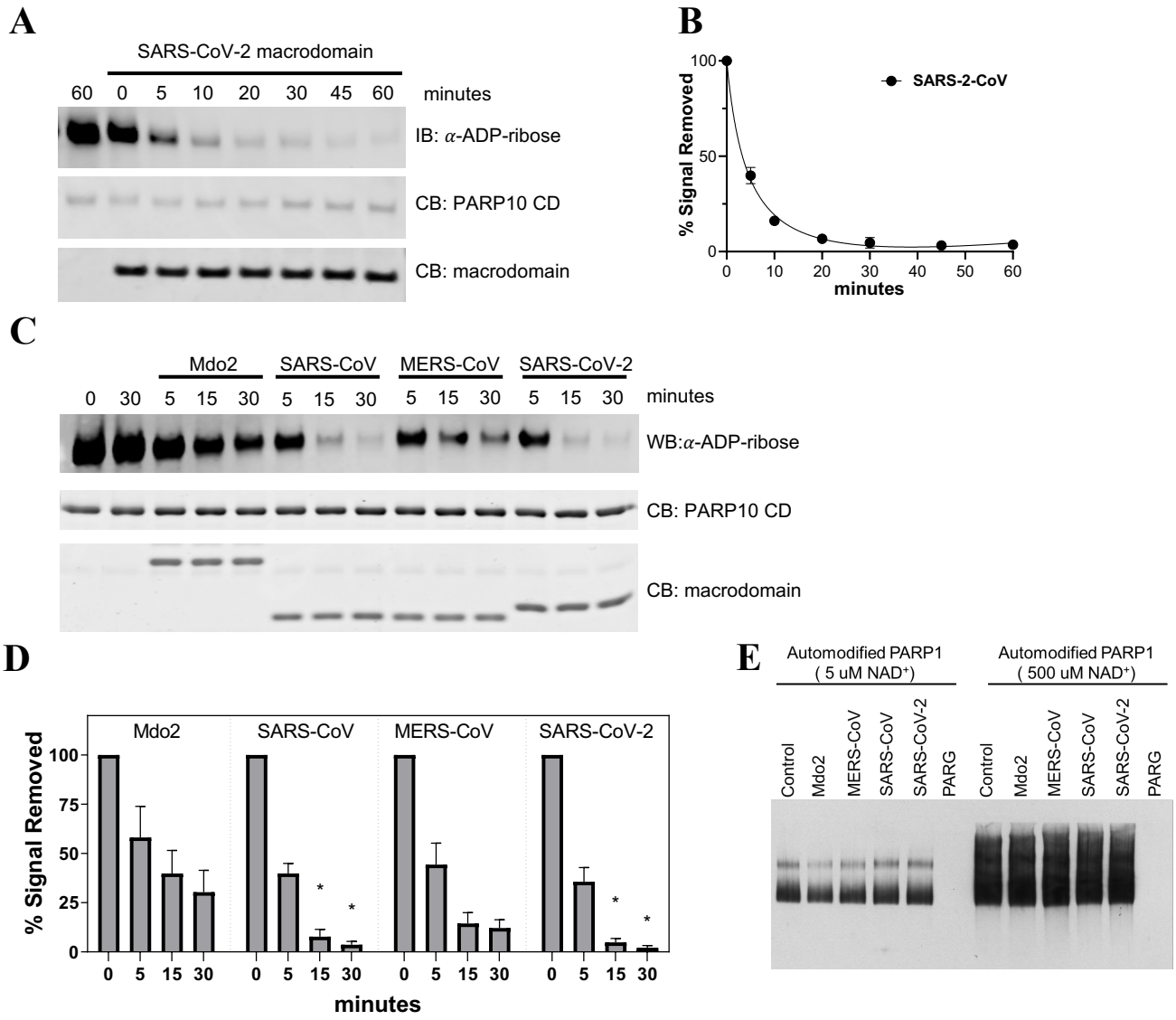

Figure 6. SARS-CoV-2, SARS-CoV, and MERS-CoV Mac1 proteins are potent ADP-ribosylhydrolases. **A,C)** The SARS-CoV-2 macrodomain **(A)** or multiple macrodomain proteins **(C)** were incubated with MARylated PARP10 CD *in vitro* for the indicated times at 37°C. ADP-ribosylated PARP10 CD was detected by immunoblot (IB) with anti-ADP-ribose antibody (Millipore-Sigma MAB1076). Total PARP10 CD and macrodomain protein levels were determined by Coomassie Blue (CB) staining. PARP10 CD incubated alone at 37°C was stopped at 0, 30 or 60 minutes. **B,D)** level of de-MARylation was measured by quantifying band intensity using Image J software. Intensity values were plotted and fit to a non-linear regression curve **(B)** or as bar graphs representing the means with error bars representing standard deviation **(D)**. Results in **A** and **C** are representative experiments of two and three independent experiments, respectively. Data in **B** and **D** represent the combined results of two and three independent experiments, respectively. Asterisks indicate statistical significance between these samples and the same timepoint from samples treated with Mdo2. **(E)** PAR hydrolase assays were performed with PARP1 either extensively poly-ADP-ribosylated (500 μM NAD^+) or partially poly-ADP-ribosylated (5 μM NAD^+) to produce oligo-ADP-ribose. Macrodomains were incubated with both automodified PARP1 substrates for 1 hour. PAR was detected by Western blot with the anti-PAR antibody 96-10. PARG (catalytically active 60 kD fragment) was used as a positive control. The results are representative of at least 2 independent experiments.

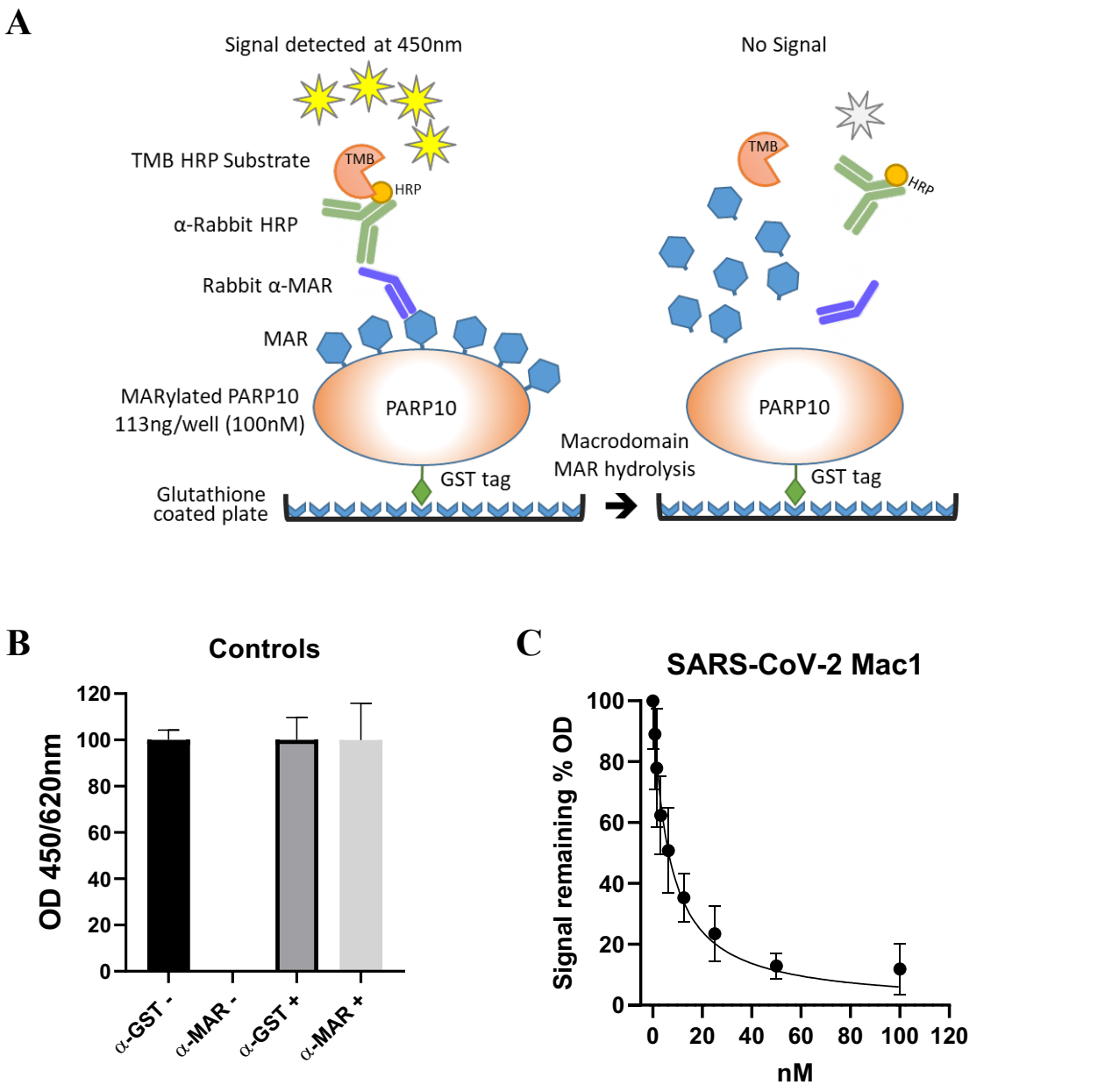

Figure 7. Development of an ELISA assay to detect de-MARylation. **A)** Cartoon schematic of the ELISA assay. ELISA plates pre-coated with glutathione and pre-blocked were used capture GST-tagged PARP10 proteins, which was used as a substrate for de-MARylation. The removal of MAR was detected by anti-MAR antibodies. **(B)** MARylated PARP10 (+) and non-MARylated PARP10 (-) with no SARS-CoV-2 Mac1 as controls were detected with anti-mono ADP-ribose antibody α-MAR (Millipore-Sigma MAB1076) or with anti-GST α-GST (Invitrogen, MA4-004). **C)** Starting at 100 nM, 2-fold serial dilutions of the SARS-CoV-2 Mac1 protein was incubated in individual wells with MARylated PARP10-CD for 30 min. at 37°C**.** The graph represents the combined results of 3 independent experiments.